

Monthly Weather Review

Characterising the local and intense water cycle during a cold air outbreak in the Nordic Seas --Manuscript Draft--

Manuscript Number:	MWR-D-18-0172
Full Title:	Characterising the local and intense water cycle during a cold air outbreak in the Nordic Seas
Article Type:	Article
Corresponding Author:	Lukas Papritz, PhD ETH Zürich Zürich, SWITZERLAND
Corresponding Author's Institution:	ETH Zürich
First Author:	Lukas Papritz, PhD
Order of Authors:	Lukas Papritz, PhD Harald Sodemann, PhD
Abstract:	<p>Air masses in marine cold air outbreaks (CAOs) at high latitudes undergo a remarkable diabatic transformation due to the uptake of heat and moisture from the ocean surface, and the formation of precipitation. In this study, the fundamental characteristics of the water cycle during an intense and persistent, yet archetypal basin-wide CAO from Fram Strait into the Nordic Seas are analysed with the aid of the tracer enabled mesoscale limited-area numerical weather prediction model COSMO. A water budget of the CAO water cycle is performed based on tagged water tracers that follow moisture picked up by the CAO at various stages of its evolution. The atmospheric dynamical factors and boundary conditions that shape this budget are thereby analysed.</p> <p>The water tracer analysis reveals a highly local water cycle associated with the CAO. Rapid turnover of water vapor results in an average residence time of precipitating waters of about one day. Approximately one third of the total moisture taken up by the CAO falls as precipitation by convective overturning in the marine CAO boundary layer. Furthermore, precipitation efficiency increases as the CAO air mass matures and is exposed to warmer waters in the Norwegian Sea. These properties of the CAO water cycle are in strong contrast to situations dominated by long-range moisture transport that occur in the dynamically active regions of extratropical cyclones. It is proposed that CAOs in the confined Nordic Seas provide a natural laboratory for studying local characteristics of the water cycle and evaluating its representation in models.</p>

Characterising the local and intense water cycle during a cold air outbreak in the Nordic Seas

3 Lukas Papritz*

4 *Geophysical Institute, University of Bergen and Bjerknes Centre of Climate Research, Bergen,*
5 *Norway*

6 Harald Sodemann

7 *Geophysical Institute, University of Bergen and Bjerknes Centre of Climate Research, Bergen,*
8 *Norway*

⁹ *Corresponding author address: now at Institute for Atmospheric and Climate Science, ETH

¹⁰ Zürich, Universitätsstrasse 16, 8092 Zürich, Switzerland

¹¹ E-mail: lukas.papritz@env.ethz.ch

ABSTRACT

12 Air masses in marine cold air outbreaks (CAOs) at high latitudes undergo
13 a remarkable diabatic transformation due to the uptake of heat and moisture
14 from the ocean surface, and the formation of precipitation. In this study, the
15 fundamental characteristics of the water cycle during an intense and persis-
16 tent, yet archetypal basin-wide CAO from Fram Strait into the Nordic Seas
17 are analysed with the aid of the tracer enabled mesoscale limited-area numer-
18 ical weather prediction model COSMO. A water budget of the CAO water
19 cycle is performed based on tagged water tracers that follow moisture picked
20 up by the CAO at various stages of its evolution. The atmospheric dynamical
21 factors and boundary conditions that shape this budget are thereby analysed.
22 The water tracer analysis reveals a highly local water cycle associated with
23 the CAO. Rapid turnover of water vapor results in an average residence time
24 of precipitating waters of about one day. Approximately one third of the total
25 moisture taken up by the CAO falls as precipitation by convective overturn-
26 ing in the marine CAO boundary layer. Furthermore, precipitation efficiency
27 increases as the CAO air mass matures and is exposed to warmer waters in
28 the Norwegian Sea. These properties of the CAO water cycle are in strong
29 contrast to situations dominated by long-range moisture transport that occur
30 in the dynamically active regions of extratropical cyclones. It is proposed
31 that CAOs in the confined Nordic Seas provide a natural laboratory for study-
32 ing local characteristics of the water cycle and evaluating its representation in
33 models.

³⁴ **1. Introduction**

³⁵ Located at the end of the North Atlantic storm track, the Nordic Seas frequently experience
³⁶ configurations of the large-scale flow that are dominated by mature and deep cyclones (Wernli
³⁷ and Schwierz 2006; Dacre and Gray 2009; Jahnke-Bornemann and Brümmer 2009). These cy-
³⁸ clones bring about strongly contrasting atmospheric conditions, varying rapidly on a timescale of
³⁹ hours to days. Incursions of warm and moist air masses from southerly latitudes in the cyclone's
⁴⁰ warm sector are accompanied by intense precipitation as the air masses ascend in the so-called
⁴¹ warm conveyor belt (e.g., Browning 1990; Madonna et al. 2014) or are steered towards the steep
⁴² orographic rise along the western Norwegian coast (Stohl et al. 2008; Azad and Sorteberg 2017).
⁴³ These warm conditions are subsequently followed by the advection of cold and dry Arctic air
⁴⁴ masses behind the cyclone's cold front. The Arctic air masses are typically colder than the un-
⁴⁵ derlying sea surface, and are therefore favourable for inducing so-called marine cold air outbreaks
⁴⁶ (CAOs; Wacker et al. 2005; Brümmer et al. 2005; Papritz and Grams 2018).

⁴⁷ CAOs are associated with a remarkably intense thermodynamic transformation of a dry and cold,
⁴⁸ stably stratified Arctic air mass into a much warmer and relatively humid, convectively unstable
⁴⁹ air mass that can bring precipitation downstream (e.g., Papritz and Spengler 2017). Due to the
⁵⁰ strong air-sea temperature contrast, CAOs give rise to intense fluxes of heat and moisture from
⁵¹ the ocean into the atmosphere (Shapiro et al. 1987; Grossman and Betts 1990; Brümmer 1996,
⁵² 1997; Wacker et al. 2005) and vigorous convective mixing (Hartmann et al. 1997; Brümmer 1999;
⁵³ Renfrew and Moore 1999). Furthermore, the high baroclinicity at the CAO's edge and the low
⁵⁴ vertical stability provide an environment favourable for the formation of mesoscale cyclones and
⁵⁵ polar lows (Businger and Reed 1989; Rasmussen and Turner 2003; Kolstad 2011). The strong
⁵⁶ uptake of moisture by the CAO air mass together with intense convective motions often results in

57 heavy snowfall (e.g., Shapiro et al. 1987; Kristovich et al. 2000; Wang et al. 2016), and it provides
58 latent energy for the intensification of mesocyclones (Rasmussen and Turner 2003; Terpstra et al.
59 2015), which in turn strongly amplify the decay of the CAO (Papritz and Pfahl 2016). In conse-
60 quence, diabatic processes play a dominant role in the evolution of CAOs. Their simulation with
61 numerical models, as well as of the related weather phenomena, relies strongly on parameterised,
62 sub-gridscale processes - more so than the simulation of other, less diabatic flows. Consequently,
63 CAOs provide a natural environment for evaluating parameterized, sub-gridscale processes. A de-
64 tailed understanding of the mechanisms driving the thermodynamic transformation of such CAO
65 air masses including their associated water cycle is, therefore, beneficial for evaluating and im-
66 proving the representation of CAOs in models as much as for our fundamental understanding of
67 the role of CAOs in the climate system.

68 From a climatological perspective, CAOs are the major drivers of heat and moisture fluxes from
69 the ocean into the atmosphere over most of the Nordic Seas (Harden et al. 2015; Papritz and
70 Spengler 2017). Compensating a substantial fraction of the freshwater input into the ocean by
71 precipitation, CAOs are, furthermore, an important cause of the relatively small magnitude of the
72 winter mean net atmospheric freshwater flux into the Nordic Seas - especially in the Greenland
73 and Iceland Seas (Segtnan et al. 2011). As CAOs are highly episodic events (e.g., Kolstad 2017),
74 small variations in their frequency of occurrence during one winter season could impose substan-
75 tial anomalies on the winter mean atmosphere-ocean buoyancy flux. This can have important
76 implications for deep convection in the ocean that contributes dense water to the lower limb of
77 the Atlantic Meridional Overturning Circulation (e.g., Marshall and Schott 1999). Consequently,
78 our aims in this study are to quantify the net footprint of the CAO water cycle in freshwater fluxes
79 (i.e., evaporation minus precipitation) and to study the dynamical factors and boundary conditions
80 that govern its spatial variations.

81 The evolution of the boundary layer structure of CAOs has been investigated extensively based
82 on observations at high latitudes (e.g., Brümmer 1996, 1997; Hartmann et al. 1997; Renfrew and
83 Moore 1999; Vihma and Brümmer 2002; Wang et al. 2016). While most of these studies did not
84 specifically focus on the water cycle, Brümmer (1997) compiled boundary layer budgets of mois-
85 ture as a function of distance from the sea ice edge for 11 CAOs from Fram Strait into the Green-
86 land and Norwegian Seas based on aircraft measurements. Complementary to such observational
87 studies, modelling studies of CAOs have been conducted on a wide range of spatial scales. They
88 include two-dimensional models to simulate the downstream evolution of the turbulent boundary
89 layer along sections extending several hundred kilometers away from the sea ice edge (e.g., Lüpkes
90 and Schlünzen 1996; Vihma and Brümmer 2002; Chechin et al. 2013), large-eddy simulations to
91 investigate the convective organization and vertical transfer of heat and moisture in a subregion of
92 the CAO (e.g., Skyllingstad and Edson 2009; Gryscha et al. 2014; Tomassini et al. 2017), and
93 mesoscale models to study the dynamical evolution and erosion of CAO air masses (Pagowski and
94 Moore 2001; Wacker et al. 2005; Papritz and Pfahl 2016). However, no systematic study has so
95 far been conducted on the fundamental characteristics of the basin-scale water cycle during CAOs,
96 and it is the major goal of this study to close this gap.

97 An especially fruitful method to diagnose the characteristics of the water cycle using numerical
98 models is by means of water vapor tracers (e.g., Bosilovich and Schubert 2002). These tracers
99 are released by evaporation from specified source regions or by transport of water vapor across
100 a certain box or surface, such as, for example, the lateral boundaries of a limited area model.
101 Previously, this water vapor tagging approach has been employed for investigating water vapor
102 isotopes (Joussaume et al. 1984; Pfahl et al. 2012), sources and recycling of precipitating waters
103 from a climatological perspective (Koster et al. 1986; Numaguti 1999; Bosilovich and Schubert
104 2002), and case studies of moisture uptake and transport contributing to heavy precipitation events

105 (Sodemann et al. 2009; Winschall et al. 2012, 2014) as well as of water vapor transport associated
106 with atmospheric rivers along the North Atlantic storm track (Sodemann and Stohl 2013).

107 In this study, we employ a limited-area numerical weather prediction model with a water vapor
108 tagging implementation to simulate the hydrological cycle associated with a major CAO that oc-
109 curred in the Nordic Seas between 24 and 27 Dec 2015. This event was one of the most intense and
110 long-lived CAOs in recent decades, while being fairly typical in terms of formation mechanisms
111 and air mass pathways. We consider the moisture budget of this CAO using tagged water tracers
112 to follow moisture that evaporated within the CAO and during different phases of its development
113 to address the following questions:

- 114 • How much water is extracted from the ocean surface during the CAO?
- 115 • How much is precipitated within the CAO area?
- 116 • How much is deposited at the surrounding topography as the CAO air masses impinge on the
117 topographic barriers?
- 118 • How much leaves the region of the CAO, impacting the budget elsewhere?

119 These aspects of the CAO’s water budget are related to the turnover rate and lifetime of water
120 vapor evaporating during this event. Furthermore, we will show that they are closely related to the
121 dynamic and thermodynamic boundary conditions, including the sea surface temperature (SST) and
122 location of the Arctic front (the sharp SST gradient separating the cold waters in the Greenland
123 and Iceland Seas from the warm waters in the Norwegian Sea, cf. Fig. 1b), as well as the sea ice
124 edge and the large-scale atmospheric flow. A set of model simulations provides insight into the
125 sensitivity of the results with respect to model resolution and parameterised convection.

126 The methodology is introduced in the subsequent section, followed by an overview of the synop-
127 tic evolution of the CAO and its linkage to low- and upper-tropospheric large-scale flow features,

128 as well as the uptake, transport and sink of vapor associated with the CAO in Section 3. In Sec-
129 tion 4 the principal characteristics of the CAO water cycle are identified and their robustness with
130 respect to model resolution is assessed in Section 5, followed by concluding remarks in Section 6.

131 **2. Methods**

132 *a. The COSMO model*

133 Simulations are performed with the mesoscale numerical weather prediction model of the Con-
134 sortium for Small Scale Modelling (COSMO; Steppeler et al. 2003; Baldauf et al. 2011) version
135 4.18. This model is in operational use at various weather services, for example the German and
136 the Swiss national weather services, and it has previously been employed for process studies of
137 CAOs and in the marginal ice zone (Wacker et al. 2005; Schröder et al. 2011; Papritz and Pfahl
138 2016), as well as for studying the water cycle (Winschall et al. 2014).

139 The COSMO model solves the thermo-hydrodynamic equations on a rotated latitude-longitude
140 grid with height-based terrain following vertical coordinate. It comprises a set of state-of-the-art
141 physical parameterizations (cf. Doms et al. 2011). This includes schemes for representing sub-
142 gridscale turbulence using a level 2.5-closure based on turbulent kinetic energy, moist convection
143 based on the mass-flux scheme by Tiedtke (1989), as well as microphysics using a one-moment
144 two category ice scheme with prognostic variables for water vapor, cloud water, cloud ice, rain,
145 and snow. The representation of microphysics in the convection parameterization is a simplified
146 version of the large-scale microphysics. For simulations at partly convection-resolving resolu-
147 tion, the model offers a non-precipitating shallow convection scheme following Tiedtke (1989),
148 that parameterizes the non-resolved portions of shallow convective mixing of heat and moisture.

149 Furthermore, a thermodynamic sea ice model with prognostic sea ice thickness and surface tem-
150 perature is used (Schröder et al. 2011).

151 For the purpose of studies of air-sea interaction processes in CAOs, the Coupled Ocean-
152 Atmosphere Response Experiment bulk air-sea heat and momentum flux parameterization
153 (COARE; Fairall et al. 1996, 2003) has been added to the COSMO model (cf. Papritz and Pfahl
154 2016). The transfer of heat and momentum parameterized with this scheme has been validated
155 against and compares particularly well with in-situ observations at high wind speeds of up to
156 20 m s^{-1} (Fairall et al. 2003; Cook and Renfrew 2015). In this study we use the COARE param-
157 eterization over open ocean grid cells, while over land and sea ice the parameterization by Louis
158 (1979) is employed.

159 *b. Water vapor tagging*

160 The idea of water vapor tagging is to extend the model by a secondary water cycle using trac-
161 ers that represent water from specified sources without affecting the primary prognostic fields in
162 the model. Here, we use the tagging implementation for the COSMO model of Winschall et al.
163 (2014), building on previous work by Sodemann et al. (2009). The secondary water cycle com-
164 prises a complete set of prognostic tracer variables for the five water species represented in the
165 model, i.e., water vapor, cloud water, cloud ice, rain water, and snow. The tracers are released
166 via the advection across the lateral boundaries into the model domain and the evaporation from
167 the surface in specifically defined regions. Likewise, sinks of the tracers are the advection out of
168 the model domain and precipitation within the domain. The prognostic tracer fields undergo the
169 same resolved and sub-gridscale processes as the prognostic fields from the primary water cycle,
170 but they do not affect the simulated meteorology. The transfer rates required for phase changes

171 between tracer species are taken as proportional to the fraction of tagged water represented by the
172 tracer times the total transfer rate obtained from the primary water cycle (Sodemann et al. 2009).

173 In this study seven distinct tracers are introduced to investigate the CAO water cycle. These
174 CAO tracers represent water entering the domain via evaporation from the ocean surface into
175 the originally essentially dry CAO air mass. To identify the CAO air mass, we use the air-sea
176 potential temperature difference $\theta_{SST} - \theta_{900}$, with θ_{SST} and θ_{900} denoting potential SST and po-
177 tential temperature at 900 hPa, respectively. This follows previous studies that employed variants
178 of $\theta_{SST} - \theta_{900}$ for the identification of marine CAOs (e.g., Bracegirdle and Gray 2008; Kolstad
179 2011; Fletcher et al. 2016; Papritz and Spengler 2017). Positive values of this CAO index indi-
180 cate an air mass that is colder than the underlying sea surface. Here, we define the evaporation
181 region of the CAO tracers as the area where $\theta_{SST} - \theta_{900}$ exceeds 4 K. This selects moderate to
182 very strong CAOs, while neglecting regions where the air-sea temperature contrast is only weakly
183 positive, with correspondingly weak upward surface heat fluxes (cf. Papritz and Spengler 2017).

184 The evaporation region is updated with each model timestep and therefore follows the evolution of
185 the CAO. To make sure that only evaporation into the main CAO air mass originating from Fram
186 Strait is considered, the evaporation region of the CAO tracers is limited to the area poleward of
187 60°N and eastward of 45°W (cf. black frame Fig 1b).

188 An overview of the time windows during which the CAO tracers are released via evaporation
189 from the ocean surface is given in Fig. 2. After their respective release windows all tracers are
190 carried through the entire remaining model integration. A new CAO tracer is initialized every
191 12 h until 1200 UTC 26 Dec (+72 h), thus yielding six CAO tracers that are released in 12-hourly
192 intervals. An additional seventh CAO tracer is defined for the time after 1200 UTC 26 Dec (+72 h;
193 blue and green bars, Fig. 2). Finally, two more tracers are introduced to (i) represent water that is
194 initially present in the model domain (gray bar, Fig. 2) and (ii) water newly entering the domain

195 during the simulation via advection across the lateral boundaries and via evaporation from land,
196 sea ice, and ocean outside of the CAO evaporation region (red bar, Fig. 2).

197 This setup should in principle allow to represent all water within the primary water cycle by the
198 tracers. Due to numerical inconsistencies, however, minor differences between tagged and total
199 water can occur (Sodemann et al. 2009; Sodemann and Stohl 2013). Throughout all simulations,
200 these differences are always less than 1 % of the total vapor and precipitation, respectively.

201 To obtain an estimate of the atmospheric residence time, i.e., the atmospheric age of precipitating
202 waters, tagged precipitation is assigned to 12-hourly bins according to the maximum time that
203 could have occurred since evaporation given the 12-hourly release intervals of the tracers. For
204 example, precipitation at $t = 18\text{h}$ that evaporated from the ocean surface between 0h and 12h
205 could have evaporated 6 h to 18 h ago and is therefore assigned to the second bin (evaporation less
206 than 24 h ago), whereas precipitation that evaporated between 12h and 18h is assigned to the first
207 bin (evaporation less than 12 h ago). Accordingly, these estimates represent upper limits for the
208 residence time and the actual values may be lower.

209 *c. Model configuration*

210 Numerical models in general have difficulties adequately simulating the convective and turbulent
211 motions in CAOs at grid-spacings of several kilometers, i.e., in the so-called convective gray zone
212 (Field et al. 2017; Tomassini et al. 2017). Consequently, a set of simulations at four different
213 grid-spacings ranging from $0.2^\circ \times 0.2^\circ$ to $0.02^\circ \times 0.02^\circ$ is performed to assess the robustness of
214 the identified characteristics of the CAO water cycle in regard of grid-spacing. Table 1 gives an
215 overview of the simulations and corresponding model configurations. While for the COSMO 0.2°
216 to COSMO 0.05° simulations the full Tiedtke (1989) convection scheme is used, two simulations
217 at a grid-spacing of $0.02^\circ \times 0.02^\circ$ are performed, one with explicit convection only (COSMO 0.02°

218 nc) and one with the shallow convection scheme active (COSMO 0.02° sc). Operational analyses
219 from the European Centre for Medium-Range Weather Forecasts (ECMWF) at a 6-hourly interval
220 serve as initial and boundary conditions for the COSMO 0.2° , COSMO 0.1° , and COSMO 0.05°
221 simulations. The analyses are interpolated onto the rotated model grid with their North Pole chosen
222 such that the equator runs across the model domain, i.e., the pole is located at 16°N and 170°E in
223 geographical coordinates (cf. Fig. 1a for domain). The simulations are initialized at 1200 UTC
224 23 Dec about 12 h before the CAO air mass is advected over open ocean (see Section 3) and the
225 model is subsequently integrated for 144 h.

226 For computational reasons the COSMO 0.02° simulations are run on a smaller domain that is
227 nested into the COSMO 0.05° domain (red box Fig. 1a). The initial and boundary conditions for
228 these simulations are taken from the hourly output of the COSMO 0.05° simulation and interpo-
229 lated onto the nested grid with its North Pole at 20°N and 160°E in geographical coordinates. For
230 simplicity, tracers from the water vapor tagging are not prescribed from the COSMO 0.05° simula-
231 tion at the domain boundaries. Instead, moisture advected into the nested domain is considered as
232 not originating from the CAO. Since the domain covers most of the region along the sea ice edge
233 where CAO air masses are advected over open ocean and there is only weak recirculation of CAO
234 air masses out and subsequently again into the domain (cf. Section 3), only a negligible amount
235 of CAO moisture is erroneously considered as non-CAO moisture due to this simplification. The
236 COSMO 0.02° simulations are initialized at 1500 UTC 23 Dec and integrated for 81 h until 0000
237 UTC 27 Dec. Consequently, the release window of the first CAO tracer is only 9 h such that the
238 CAO tracers remain synchronized in all simulations (lower bars Fig. 2).

239 In all simulations, the evolution of the large-scale horizontal structure and thermodynamic pro-
240 files of the CAO are in close agreement with operational analyses from the ECMWF (not shown).
241 Throughout this study, the COSMO 0.05° simulation will serve as the reference simulation. It will

²⁴² also be used to discuss the evolution of the CAO and establish the principal characteristics of the
²⁴³ CAO water cycle in Sections 3 and 4. Based on the additional simulations, the robustness of these
²⁴⁴ characteristics will be assessed in Section 5.

²⁴⁵ **3. Evolution of the CAO event**

²⁴⁶ *a. Synoptic overview*

²⁴⁷ In this section, we will give an overview of the synoptic evolution of the CAO based on ERA-
²⁴⁸ Interim reanalysis data (Fig. 3) and the COSMO 0.05° simulation (Fig. 4). To that end, we will
²⁴⁹ visualize the pool of cold air in the interior Arctic and the export of the CAO air mass into the
²⁵⁰ Nordic Seas in a quasi-Lagrangian manner by depicting the evolution of the mass located below
²⁵¹ a specific isentropic surface θ_T and the ground, the so called cold air mass (Iwasaki et al. 2014;
²⁵² Papritz and Pfahl 2016). The choice of θ_T is informed by the maximum SST to which the CAO
²⁵³ air mass is exposed while in the Norwegian Sea, which amounts to slightly more than 280 K (cf.
²⁵⁴ Fig. 1b). All air leaving the interior Arctic with a potential temperature below 280 K has the
²⁵⁵ possibility to contribute to the CAO. We thus use a threshold of $\theta_T = 280$ K.

²⁵⁶ The formation of the CAO and its evolution are closely linked to a positive potential vorticity
²⁵⁷ anomaly in the lower stratosphere, which is characterised by a low-lying and cold tropopause
²⁵⁸ (Fig. 3a) and an upward doming of isentropic surfaces below (i.e., anomalously cold air; cf.
²⁵⁹ Hoskins et al. 1985). This feature has its origin over northwestern Greenland (Fig. 3a), which is
²⁶⁰ a region favourable for the genesis of such lower stratospheric positive potential vorticity anom-
²⁶¹ alies (Kew et al. 2010). It subsequently translates towards Fram Strait and into the Greenland Sea
²⁶² (Fig. 3b), accompanied by the advection of particularly cold air across the sea ice edge into the
²⁶³ Nordic Seas underneath. The latter is evident from the thick tongue of cold air that forms in the

264 Nordic Seas (red; Figs. 4a-c), as well as an increasing air-sea potential temperature contrast (red
265 contours). A persistent and intense lower tropospheric transport of cold air is established by the
266 strengthening of the pressure gradient on the rearward side of an extensive surface trough in the
267 Norwegian Sea (gray contours and green arrows; Fig. 4b). Furthermore, a mesoscale cyclone west
268 of the Svalbard archipelago episodically enhances the transport of cold air over Fram Strait during
269 the initial stage of the CAO.

270 As evident from the lowering of the tropopause to nearly 500 hPa, the further evolution of the
271 CAO is steered by the filamentation and strengthening of the upper-level feature, and the formation
272 of an elongated dome of cold air mass underneath that stretches from the sea ice edge across the
273 Nordic Seas all the way towards Norway (Figs. 3c and 4c). Consequently, the air-sea potential
274 temperature difference attains values well above 12 K over large portions of the Nordic Seas -
275 indicative of a very intense CAO accompanied by surface turbulent heat fluxes well in excess of
276 600 W m^{-2} (not shown). The cold front that marks the edge of the CAO and extends throughout
277 the entire troposphere makes landfall in Norway on early 26 Dec (Fig. 4c). While the upper-
278 level feature and the cold air mass tongue subsequently extend further across Scandinavia and
279 translate north-eastwards (Figs. 4d and 3d), the strong lower tropospheric pressure gradient across
280 the Nordic Seas and the associated rapid export of cold air from the interior Arctic via Fram Strait
281 are sustained until 27 Dec (Fig. 4d).

282 The co-evolution of the upper-level feature and the CAO suggests a dynamical coupling of the
283 upper-level flow and the formation of the CAO. In particular, the eastward propagation of the
284 upper-level front that is associated with the lowering of the tropopause induces lifting and conse-
285 quently reinforces the surface trough in the Norwegian Sea and the development of the mesocy-
286 clone west of Svalbard, thus enhancing the pressure gradient that steers the export of the cold air
287 from the interior Arctic. A similar coupling of upper and low-level flow during CAO formation

288 has previously been noted in a case study of a CAO in the South Pacific (Papritz and Pfahl 2016).
289 In climatological terms, the formation of the CAO on the rearward side of a surface trough with its
290 center in the Norwegian and Barents Seas corresponds to one of the archetypal synoptic configu-
291 rations leading to CAOs that extend across the entire basin of the Nordic Seas (cf. Kolstad et al.
292 2009; Papritz and Grams 2018). Furthermore, the export of cold air from the interior Arctic via
293 Fram Strait and the subsequent flow across the Arctic front towards the Norwegian coast, is one of
294 the principal pathways taken by air masses that contribute to CAOs in the Nordic Seas (Papritz and
295 Spengler 2017). From this climatological perspective, this CAO is a typical one for that region.
296 The persistence of the cold air mass outflows from the Arctic implies, however, that a particularly
297 large portion of the Nordic Seas was affected by this CAO at a time.

298 *b. From evaporation to precipitation*

299 One of the salient features of polar cold air masses favourable for inducing CAOs is their initial
300 dryness, thus leading to the strong uptake of moisture once the air mass is exposed to the ocean
301 followed by the formation of convective clouds and precipitation. This is exemplarily illustrated by
302 the AVHRR satellite image (Fig. 5a) valid at 1935 UTC 25 Dec showing cloud streets that develop
303 off the sea ice edge, as well as a transition towards cellular convection. Furthermore, Fig. 6 shows
304 snapshots of evaporation, total column vapor, and precipitation at 00 UTC 26 Dec (+60 h). In the
305 Arctic and over the Nordic Seas - collocated with the CAO (purple) - total column vapor is strongly
306 depleted with values well below 2 mm (Fig. 6b). It is within the CAO, however, where the strongest
307 evaporation rates in the study region occur (Fig. 6a). At the same time, marine precipitation
308 collocated with the CAO is also prevalent (Fig. 6c). Furthermore, intense precipitation associated
309 with orographic lifting is found along the coasts of Norway and south-eastern Greenland. While
310 a linkage between precipitation over Norway and the uptake of moisture by the CAO air mass

311 is rather manifest, this is less obvious for precipitation along the southeast coast of Greenland.

312 In the following, we will make use of the water vapor tracers as introduced in Section 2 to link

313 evaporation into the CAO air mass to precipitation.

314 First, we illustrate the evolution of the water cycle associated with the CAO throughout the

315 previously described life-cycle of the CAO. In particular, we investigate where water vapor picked

316 up by the CAO contributes to precipitation. Figure 7 gives an overview of hourly accumulated

317 evaporation into the CAO air mass (left column), total column tagged CAO vapor (middle column),

318 and hourly accumulated tagged CAO precipitation (right column). The terms *tagged CAO vapor*

319 and *tagged CAO precipitation* refer to the portions of water vapor and precipitation, respectively,

320 that are associated with the CAO tracers. By definition, this represents water that has previously

321 evaporated into the CAO air mass.

322 Initially, the most intense evaporation into the CAO air mass of up to 0.5 mm h^{-1} occurs in a

323 narrow band off the sea ice edge and over the tongue of relatively warm waters west of Svalbard. It

324 declines to less than 0.3 mm h^{-1} further into the basin (Figs. 7a, d). Convective overturning leads to

325 the onset of tagged CAO precipitation slightly downstream of the sea ice edge (Figs. 7c, f). As the

326 CAO air masses are advected across the Arctic front over the warm waters of the Norwegian Sea,

327 the evaporation rates increase again and reach values as high as near the sea ice edge. In contrast

328 to the band along the sea ice edge, however, these high values extend much further downstream

329 (Figs. 7g, k). Furthermore, this increase of evaporation is concomitant with a sharp increase of

330 tagged CAO precipitation from rather uniform values of around 0.1 mm h^{-1} in the Greenland Sea

331 to locally more than 1 mm h^{-1} in the Norwegian Sea (e.g., Fig. 7i). Consequently, total column

332 tagged CAO vapor does not show such pronounced changes downstream of the Arctic front as

333 evaporation and precipitation; instead it increases nearly linearly with distance from the sea ice

334 edge to close to 4 mm near the Norwegian coast (Figs. 7e, h, l). These findings suggest a strong

335 influence of the SST distribution on the water cycle and, in particular, a more vigorous turnover
336 of water vapor over the warm waters of the Norwegian Sea compared to the Greenland Sea that
337 limits the growth of column tagged CAO vapor.

338 Important parts of the Nordic Seas are bounded by steep orographic rises. Hence, a major
339 portion of CAO precipitation occurs over land induced by orographic lifting when CAO air masses
340 impinge on the coast. Indeed, high rates of tagged CAO precipitation are found along the coast of
341 central and northern Norway, but also along south-eastern Greenland (Fig. 7i) with the latter being
342 related to a south-westward excursion of tagged CAO vapor during the early phase of the CAO
343 (Figs. 7e, h). This poses the question about what role moisture input and precipitation efficiency
344 over the ocean play in controlling the amount of precipitation along the orographic rises.

345 Figure 8 shows the contributions of CAO and non-CAO vapor to marine precipitation in the
346 Greenland, Iceland and Norwegian Seas and over central to northern Norway (GIN and NOR
347 boxes, respectively, of Fig. 1a). Colors indicate tagged CAO vapor released in the respective time
348 frames and gray shadings depict tagged vapor initially present and of non-CAO origin. The con-
349 tribution of tagged CAO vapor to marine precipitation in the GIN region (Fig. 8a) increases gradu-
350 ally from the start of the simulation. Contributions increase as the more intense CAO precipitation
351 downstream of the Arctic front sets in at 12 UTC 24 Dec (+24 h). Marine CAO precipitation peaks
352 and reaches a plateau around 00 UTC 26 Dec (+60 h) when the cold front makes landfall along
353 the Norwegian coast and the CAO air mass occupies most of the GIN Seas. During that plateau
354 phase, the bulk of precipitation in the GIN region is of CAO origin (> 80 %). After 12 UTC 26
355 Dec (+72 h) the continuous supply of CAO air masses decreases and marine CAO precipitation in
356 the GIN region declines.

357 CAO precipitation in the NOR region (Fig. 8b) sets in with the landfall of the cold front and
358 peaks at 00 UTC 26 Dec (+60 h) with the highest precipitation rates throughout the entire event.

359 Interestingly, most of the cold frontal precipitation in the NOR box is of CAO origin, whereas
360 precipitation of waters of non-CAO origin in the ascent regions ahead of the front contributes
361 substantially less. This may be related to a weakening of the front due to the frontolytic effect of
362 surface sensible heat fluxes (Spensberger and Sprenger 2017). After the passage of the cold front,
363 precipitation in the NOR region levels off at a lower and fairly constant value while the CAO air
364 mass is lifted over the orographic rise (Fig. 8b). After 00 UTC 27 Dec (+84 h) the dome of cold
365 air translates into the Barents Sea and precipitation decreases.

366 In summary, the synoptic analysis points towards a highly local water cycle with relatively rapid
367 turnover of vapor established during the life-cycle of the CAO over large portions of the Nordic
368 Seas. In the following section, we aim to shift the focus away from this synoptic view towards a
369 space and time integrated perspective on the water cycle during this CAO event with the goal to
370 corroborate these qualitative findings more quantitatively.

371 **4. The CAO water cycle**

372 *a. Integral characteristics*

373 A quantitative account of the net input of vapor into the atmosphere during this CAO event is
374 obtained from the domain integrated evaporation into the CAO air mass and tagged CAO precip-
375 itation (Fig. 9). In this section we focus on the $0.05^\circ \times 0.05^\circ$ simulation only (solid lines). The
376 rate of evaporation into the CAO air mass (orange) increases rapidly, peaks after 1200 UTC 25
377 Dec (+48 h), and declines shortly after 1200 UTC 26 Dec (+72 h, Fig. 9a). Tagged CAO precipi-
378 tation (blue) peaks about 12 h after evaporation and reaches a plateau sustained for nearly one day
379 until 0000 UTC 27 Dec (+84 h). Subsequently, precipitation largely compensates the additional
380 moisture input by evaporation as evident from the closeness of the orange and blue lines. Con-

sequently, the net input of vapor remains small after that time. Initially, most of the tagged CAO precipitation is collocated with the CAO masks (compare green and blue lines). As of 1200 UTC 25 Dec (+48 h), however, more and more of the CAO vapor is lost via precipitation in dynamical weather systems outside of the CAO and along the orographic boundaries of the Nordic Seas. The total evaporation into the CAO air mass amounts to $65 \cdot 10^{12}$ kg, of which $22 \cdot 10^{12}$ kg fall as precipitation within the CAO mask corresponding to 34 % of the total uptake (Fig. 9b). Thus, the net injection of moisture by the CAO of $43 \cdot 10^{12}$ kg corresponds to nearly 7 % of the integrated water content of the atmosphere poleward of 40°N ($\approx 6.4 \cdot 10^{14}$ kg) as estimated from the ERA-Interim reanalysis. An additional $20 \cdot 10^{12}$ kg or 30 % is lost via precipitation outside of the CAO.

Brümmer (1997) computed composite water budgets of 11 CAO cases based on aircraft measurements (8 CAOs from Fram Strait and 3 in the Norwegian Sea). That study estimated the efficiency of precipitation formation by the CAO, expressed as the ratio of precipitation to evaporation, to be 25 % to 33 % up to 150 km from the sea ice edge and values in excess of 50 % further downstream. Given that the CAO investigated here extends from the sea ice edge across the entire Nordic Seas and thus occupies a major portion of the warm waters in the Norwegian Sea, the value of 34 % found here appears rather low in comparison, even though it has been computed from evaporation and precipitation integrated over the entire event, as well as in space. We therefore shed more light on the spatial variation of the precipitation efficiency by considering the footprints of the CAO event in accumulated evaporation and precipitation.

Evaporation into the CAO air mass accumulated over the CAO event features clear local maxima (Fig. 10a). A first prominent maximum is located along the sea ice edge extending from north of Svalbard into the Greenland Sea and with values in excess of 20 mm. A second maximum of the same magnitude is found on the warm side of the Arctic front (gray contour). The dominant cause for the evaporation maximum over Fram Strait and in the Greenland Sea lies in the sustained

405 nature of the off ice flow throughout the entire event (i.e., Fig. 4) leading to less intense but more
406 persistent instantaneous evaporation rates than in the Norwegian Sea (cf. Fig. 7). Furthermore,
407 the existence of an ice-sea-breeze circulation could contribute further towards enhanced fluxes
408 in the vicinity of the sea ice edge (e.g., Chechin et al. 2013). Despite the high instantaneous
409 evaporation rates, the rather episodic passage of the CAO air mass over the Norwegian Sea (i.e.,
410 Fig. 4) leads to a decrease in the accumulated evaporation from the Arctic front towards the coast
411 of Norway. Consequently, evaporation accumulated during the event is less over the warm waters
412 in the Norwegian Sea than over the cold waters near the sea ice edge in the Greenland Sea.

413 Accumulated CAO precipitation increases downstream of the Arctic front with values of more
414 than 12 mm over much of the eastern Norwegian Sea (Fig. 10b). This increase reflects the consid-
415 erably stronger precipitation rates there compared to the upstream region. Similarly high values of
416 accumulated precipitation are also found in an adjacent band inland of the west coast of Norway
417 and in south-eastern Greenland. An eminent peak in total precipitation occurs between the sea
418 ice edge and Svalbard, where, due to the continuous passage of CAO air masses weak but persis-
419 tent precipitation leads to an accumulated precipitation of slightly more than 12 mm. This peak is
420 shifted slightly downstream of the evaporation maximum near the sea ice edge.

421 We obtain the footprint of the CAO in net freshwater fluxes, defined as evaporation minus pre-
422 cipitation, by combining accumulated evaporation and precipitation. The largest positive values
423 of the freshwater flux associated with the CAO, thus, ensue near the sea ice edge north-west of
424 Svalbard and in the Greenland Sea, as well as on the warm side of the Arctic front (Fig. 10c).
425 The freshwater flux declines considerably downstream of these maxima as precipitation strength-
426 ens such that over the eastern part of the Norwegian Sea it reaches nearly neutral or even slightly
427 negative values. It therefore seems that precipitation from water picked up by the CAO earlier and

428 further upstream to a large degree compensates the strong evaporation rates over the warm waters
429 in the Norwegian Sea.

430 The efficiency of precipitation formation (the ratio of precipitation falling in collocation with
431 the CAO mask and evaporation into the CAO air mass) has the lowest values of less than 10 %
432 near the sea ice edge, while steadily increasing downstream with values in the eastern Norwegian
433 Sea largely exceeding 50 % (Fig. 10d). The ratio of 34 % obtained previously from area integrated
434 quantities is, therefore, representative of the values near the Arctic front in the middle of the
435 basin. Between the sea ice edge and Svalbard there is another region with ratios larger than 50 %,
436 which occurs due to the large amount of CAO precipitation. Since this is the region where 8
437 of the 11 CAOs described in Brümmer (1997) occurred, it is likely that the values derived from
438 their composite water budget are representative of this particular region. In fact, our estimates
439 are in good agreement with the increase of the ratio from 0.25 near the sea ice edge north-west of
440 Svalbard to 0.6 about 300 km downstream as found by Brümmer (1997). On the scale of the Nordic
441 Seas, however, the ratio increases less rapidly with distance from the sea ice edge. We suggest that
442 this effect is owed to the large SST gradient related to the Arctic front and the associated increase
443 of the evaporation rates.

444 *b. Local nature of the water cycle and rapid overturning*

445 The local nature of the water cycle is emphasized by the spatial footprints of accumulated evap-
446 oration and precipitation of the individual CAO tracers that are released in 12-hourly intervals.
447 Figure 11 depicts these footprints for the three tracers that contribute most to precipitation in the
448 GIN and NOR regions until 0000 UTC 27 Dec (+84 h), namely the tracers that are released be-
449 tween 36 - 48 h, 48 - 60 h, and 60 - 72 h (see Fig. 8). Evaporation is accumulated over the 12-hourly
450 window during which the tracer is released, while precipitation is accumulated from the start of

451 the tracer release window until 0000 UTC 27 Dec. The accumulated evaporation in the Greenland
452 Sea reaches values of 5 mm between the sea ice edge and Svalbard, and is quite similar for all
453 three tracers.

454 Major differences exist, however, downstream of the Arctic front in the Norwegian Sea. Mois-
455 ture uptake by the tracer released between 36 - 48 h is confined to the region west of the position of
456 the cold front at the end of the tracer release window (1200 UTC 25 Dec, Fig. 11a), such that the
457 eastern Norwegian Sea does not contribute. Accumulated precipitation of 1 - 3 mm, in contrast,
458 extends further downstream over the entire Norwegian Sea and spreads along the coast of Norway
459 (Fig. 11b). This is a hallmark of the accumulation of CAO vapor on the rearward side of the cold
460 front - vapor that contributes to frontal precipitation when the front weakens while passing the
461 eastern Norwegian Sea.

462 The water cycle associated with the two subsequently released tracers appears more spatially
463 confined. The accumulated evaporation increases rapidly downstream of the Arctic front and
464 reaches 5 - 6 mm in most of the Norwegian Sea (Figs. 11c, e). Furthermore, there is a pronounced
465 increase of precipitation to values of more than 4 mm over a widespread area in the Norwegian Sea
466 with maxima displaced slightly to the east of maxima in evaporation (Figs. 11d, f). The spatially
467 confined patterns in accumulated evaporation and precipitation, in particular the closeness of local
468 maxima in evaporation and precipitation, clearly point towards a highly localized nature of the
469 water cycle, and consequently a rapid overturning of moisture.

470 The intensity and speed of the overturning of moisture within the CAO air mass is substantiated
471 by the short residence time of the vapor in the atmosphere, i.e., the time between evaporation
472 and precipitation. Figure 12 shows the distribution of the residence time as estimated from the
473 CAO tracers released in 12-hourly intervals (see Section 2). Note that the 12-hourly bins for
474 the residence time are exclusive, i.e., all CAO precipitation in one of the boxes is attributed to

475 exactly one bin. Due to the 12-hourly intervals between the release of new tracers, some of the
476 precipitation with a residence time of, for example, less than 24 h may in fact have evaporated less
477 than 12 h ago. This estimate, therefore, presents an upper limit for the residence time. Figure 12a
478 shows that more than 45 % of the CAO precipitation in the GIN region has evaporated less than
479 12 h before, and another about 40 % less than 24 h before with a sharp drop in the contributing
480 fraction for residence times larger than one day. This sharp drop for residence times larger than
481 one day is also present in CAO precipitation over Norway, though with a shift towards higher
482 residence times (Fig. 12b). The largest contribution of nearly 50 % is from the category with
483 evaporation less than 24 h ago, and about 35 % for 12 h residence time. As the cold front makes
484 landfall with pronounced precipitation, it deposits water that evaporated in the early phase of
485 the CAO and accumulated on the rearward side of the front, contributing to the observed shift
486 in residence times. Given that these estimates present upper limits, we conclude that the mean
487 residence time of precipitating CAO waters is clearly below 24 h. The water cycle associated with
488 CAOs is, therefore, highly localized and characterised by very rapid overturning on a timescale of
489 less than a day.

490 5. Sensitivity to model resolution

491 As previous modelling studies of the convective boundary layer of CAOs with horizontal grid-
492 spacings in the convective gray zone (i.e., a few kilometers) have shown, substantial differences
493 in the boundary layer evolution may arise in simulations with different model resolutions due to a
494 lack of scale awareness of the parameterizations for convection and turbulent mixing (e.g., Field
495 et al. 2017; Tomassini et al. 2017). Such deficiencies may also impact the representation of the
496 hydrological cycle. We therefore assess the robustness of the previously identified integral char-
497 acteristics of the hydrological cycle of the CAO, as well as its footprint in freshwater fluxes, using

498 model simulations at grid-spacings spanning the range from $0.2^\circ \times 0.2^\circ$ to convection permitting
499 $0.02^\circ \times 0.02^\circ$.

500 First, we compare the domain-integrated hydrological cycle of the three coarsest simulations
501 (Figure 9). As reflected in evaporation into the CAO air mass and CAO precipitation, there is a
502 close agreement between the reference simulation ($0.05^\circ \times 0.05^\circ$, solid) and the two simulations
503 with larger grid-spacing ($0.1^\circ \times 0.1^\circ$ and $0.2^\circ \times 0.2^\circ$, dashed and dotted). While the total amount
504 of evaporation by the CAO is nearly identical for all simulations (differences of less than 1.2 %
505 between the simulations with grid-spacings of $0.2^\circ \times 0.2^\circ$ and $0.05^\circ \times 0.05^\circ$), the total amount
506 of CAO precipitation increases by about 6 % as the grid-spacing decreases. As also supported by
507 the slightly lower residence times, this indicates a modestly more rapid turnover of CAO vapor at
508 lower grid-spacings (cf. Fig. 12).

509 Second, we consider in Fig. 13 the spatial imprints in 78 h accumulated freshwater fluxes as
510 in Fig. 10c. The spatial patterns are consistently simulated in terms of location and shape of the
511 spatial structure along the sea ice edge west of Svalbard and in the Greenland Sea. Simulations
512 also agree regarding the location of the local maximum on the warm side of the Arctic front. Clear
513 differences in magnitude are, however, apparent downstream of the Arctic front, especially along
514 the coast and over Norway, and in the finer scale structures.

515 Spatial integrals of the accumulated precipitation associated with each of the individual tracers
516 over the Greenland, Iceland and Norwegian Seas region (GIN box in Fig. 1a; Fig. 14a) and central
517 to northern Norway (NOR box Fig. 1a; Fig. 14b) show that marine CAO precipitation increases as
518 grid-spacing is reduced from $0.2^\circ \times 0.2^\circ$ to $0.05^\circ \times 0.05^\circ$. This increase is mainly due to the tracers
519 that were released between 48 - 60 h, and 60 - 72 h. Equal contributions across resolution are
520 observed for tracers released earlier, which, in particular, contribute to precipitation immediately
521 behind the cold front (Fig. 14a). Thus, the differences arise mainly within the convective interior

522 of the CAO air mass, hinting at potential inconsistencies in the interplay between the convection
523 parameterization and the increasing portion of convective motions within the CAO air mass that
524 are explicitly resolved by the model (e.g., Field et al. 2017; Tomassini et al. 2017).

525 Analysis of the separate contributions of grid-scale and convective precipitation lends further
526 support to this interpretation (Table 2): The contribution of convective precipitation increases,
527 while grid-scale precipitation reduces slightly. Since the decrease of grid-scale precipitation is
528 lower than the increase of convective precipitation, it results in a net increase of CAO precipitation.
529 In comparison to the simulation at a grid-spacing of $0.2^\circ \times 0.2^\circ$, convective precipitation nearly
530 quadruples in the $0.05^\circ \times 0.05^\circ$ run, while grid-scale precipitation reduces by less than 30 % of
531 the increase in convective precipitation. Since the evaporation rates are nearly identical in all three
532 simulations (Fig. 12), an important implication of the increase of marine CAO precipitation with
533 increasing resolution is that there is less CAO vapor available that could contribute to precipitation
534 over Norway (Fig. 14b).

535 The two convection permitting simulations with a grid-spacing of $0.02^\circ \times 0.02^\circ$ show a clear de-
536 crease in CAO precipitation in the Greenland, Iceland, and Norwegian Seas (Fig. 14a), and further
537 an increase over Norway (Fig. 14b) when compared to the $0.05^\circ \times 0.05^\circ$ simulation. Marine CAO
538 precipitation decreases more strongly in the simulation with shallow convection parameterization
539 switched on. The parameterization acts to transport CAO vapor upward and potentially warmer air
540 downward, and thereby leads to a modestly more rapid growth of the depth of the CAO boundary
541 layer. This results in slightly enhanced evaporation from the ocean surface and overall less marine
542 CAO precipitation (not shown).

543 Comparing outgoing longwave radiation at 1900 UTC 25 Dec from the two convection permit-
544 ting simulations with infrared satellite imagery reveals remarkable agreement in certain details,
545 but also emphasizes discrepancies especially downstream in the Norwegian Sea (Fig. 5). In both

546 simulations cloud streets develop off the ice and there is a clear-cut transition from roll vortices
547 towards cellular convection (Figs. 5b, c), in good agreement with the satellite image (Fig. 5a).
548 Morphology and organization of the cellular convection are, however, different in the two sim-
549 ulations. Cloud cover is considerably less dense in the simulation without shallow convection
550 parameterization, in agreement with the weaker net water uptake in that simulation. Furthermore,
551 a comparison with the satellite image (Fig. 5a) suggests that the ratio between cloud free versus
552 cloudy regions may lie somewhere in between the two simulations, albeit with clearly finer cloud
553 structures than produced by either of them.

554 Based on the above analysis, we conclude that the major characteristics of the water cycle asso-
555 ciated with the CAO are robust with respect to changes to the grid-spacing. Nevertheless, quantita-
556 tive inconsistencies in the representation of the CAO water cycle are identified even at convection
557 permitting grid-spacing, and convergence is not evident as more and more of the convective mo-
558 tions are resolved with decreasing grid-spacing. This is consistent with large eddy simulations in-
559 dicating that a grid-spacing on the order of 100 m is required to properly resolve the full spectrum
560 of convective motions (Bryan et al. 2003) and it underlines the need for scale-aware parameteri-
561 zations of the non-resolved portions of convective and sub-gridscale turbulent motions to properly
562 represent CAOs in kilometer-scale models.

563 6. Concluding remarks

564 This study presents the dynamical evolution of an intense and long-lived yet typical CAO from
565 Fram Strait into the Nordic Seas that occurred 24 Dec to 27 Dec 2015. The analysis is focused
566 on an investigation of the associated evolution and characteristics of the water cycle in the Nordic
567 Seas established during that event.

568 The formation and development of the CAO were closely linked to the evolution and prop-
569 agation of an upper-level feature characterized by a low-lying tropopause that wandered from
570 north-western Greenland towards Fram Strait and from there into the Nordic Seas with a dome
571 of cold air underneath. Delimited by an initially intense cold front extending all the way to the
572 tropopause, cold air was continuously supplied from the interior Arctic for more than two days
573 and advected across the Nordic Seas. This sustained flow of originally cold and dry air masses
574 across the Nordic Seas gave rise to intense sensible and latent heat fluxes from the ocean surface,
575 leading to the strong transformation of the air mass.

576 In order to quantitatively analyse the characteristics of the water cycle during that CAO, the
577 event was investigated by means of a tracer-enabled limited area numerical weather prediction
578 model. Our main findings regarding the characteristics of the water cycle associated with this
579 CAO event are as follows:

580 1. The CAO is associated with a highly confined water cycle, with a rapid overturning of vapor
581 within the CAO air mass. This is underlined by the finding that the Norwegian Sea is the
582 dominant moisture source region for CAO precipitation along the Norwegian coast and over
583 Norway during the CAO period. During such weather situations, the Nordic Seas and the
584 surrounding topography can, thus, be considered as a natural laboratory to study the local
585 characteristics of the water cycle by models and observations.

586 2. Water vapor has a very rapid turnover within the CAO, with an average residence time of
587 about one day. This residence time is considerably smaller than the climatological residence
588 time of 3 to 4 days for vapor contributing to precipitation in the Nordic Seas as obtained from
589 trajectory analysis (Laederach and Sodemann 2016), or than the 8–10 days often considered
590 as a global average value (e.g., Bosilovich et al. 2005).

- 591 3. About one third of the total moisture taken up by the CAO falls as precipitation due to con-
592 vective overturning in the marine CAO boundary layer. Another third rains out inside the
593 model domain but unrelated to convection within the CAO, that is along the steep coastal
594 boundaries of the Nordic Seas, as well as in dynamical weather systems over ocean. The last
595 third remains as vapor in the atmosphere or is advected out of the domain. In total, this leads
596 to a net injection of vapor by the CAO¹ into the high latitude atmosphere of $43 \cdot 10^{12} \text{ kg}$ ($\sim 7\%$
597 of the atmospheric water content poleward of 40°N).
- 598 4. The water cycle is strongly modulated by the pattern of SST over the CAO region. The CAO
599 air mass is exposed to rapidly increasing SST as it crosses the Arctic front from the cold
600 Greenland Sea into the warm Norwegian Sea. Consequently, evaporation rates increase sub-
601 stantially on the warm side of the front, as does precipitation efficiency further downstream.
- 602 5. Accumulated freshwater fluxes are characterized by an excess of evaporation over precipi-
603 tation. Overall values decrease from the ice edge towards the Norwegian coast, albeit with
604 local maxima of the net vapor injection along the sea ice edge and on the warm side of the
605 Arctic front. Important factors in shaping these spatial patterns are
606 (i) the persistent outflow of very cold air masses from Fram Strait across the ice edge for
607 several days with moderate evaporation rates contrasting the rather episodic passage of the
608 CAO air masses across the Norwegian Sea where evaporation rates are substantially higher,
609 (ii) and the partial compensation of the more intense evaporation downstream of the Arc-
610 tic front in the Norwegian Sea by enhanced precipitation of CAO vapor that was picked up
611 upstream.

¹The net injection is considered to be the total evaporation into the CAO air mass minus precipitation due to convective overturning within the CAO boundary layer.

612 6. Simulations with horizontal grid-spacings ranging from $0.2^\circ \times 0.2^\circ$ to convection permitting
613 $0.02^\circ \times 0.02^\circ$ indicate that the integral characteristics of the CAO water cycle, as well as
614 the principal features of the CAO in footprints of freshwater fluxes are robustly represented
615 across resolutions. Inconsistencies exist, however, regarding the amount of marine convective
616 precipitation. Since local small-scale processes play a dominant role for the water cycle
617 during CAO situations, CAOs can serve as ideal target cases to evaluate the accuracy of the
618 representation of the water cycle and the impact of parameterised small-scale processes on
619 the performance of numerical weather prediction models.

620 The characteristics of the water cycle during episodes of CAO precipitation along the Norwegian
621 coast and over Norway are in sharp contrast to those during episodes of precipitation associated
622 with strongly ascending moist air streams (i.e., warm conveyor belts; Sodemann and Stohl 2013;
623 Pfahl et al. 2014). Both types of episodes are closely linked to the passage of cyclones: warm
624 conveyor belts are related to the warm sector of cyclones with long-range vapor transport ahead
625 of the cold front (Madonna et al. 2014; Pfahl et al. 2014) and they often represent a major sink
626 for vapor associated with an atmospheric river (Sodemann and Stohl 2013), whereas CAOs - as in
627 the present case - are linked to the cyclone's cold sector (Papritz et al. 2015; Vannière et al. 2016;
628 Papritz and Grams 2018). During periods with the frequent passage of cyclones, precipitation
629 in the Norwegian Sea and over Norway is therefore characterised by temporally highly variable
630 moisture source regions and associated uptake conditions, moisture transport, and timescale from
631 evaporation to precipitation.

632 The insights gained from this study are also relevant for the ongoing YOPP (Year of Polar Pre-
633 diction²) effort that brings major attention to this region in terms of modelling and observational
634 studies. The highly local water cycle in the Norwegian Sea recommends the region as a natural

²<http://www.polarprediction.net/>

635 laboratory of the water cycle. Testing the representation of different sub-grid scale processes, in-
636 cluding convection, in a model framework should be highly effective during such CAO situations.
637 In addition, observational studies targeting the water cycle may be particularly valuable in this
638 region. The distinct transformation of the CAO air masses due to strong latent heat fluxes cre-
639 ate situations where natural tracers of moisture source and transport based on the stable isotope
640 composition of the water vapor can be applied to validate the water cycle in models. Variations
641 in the parameter deuterium excess, for example, may allow one to identify the timing and change
642 in source conditions at coastal measurement sites (Pfahl and Sodemann 2014; Steen-Larsen et al.
643 2015). Such a comparison requires information on the water cycle in the model that is adequate for
644 evaluation with isotope measurements. The tagging approach, and its extension into a full stable
645 isotope fractionation physics package (Pfahl and Wernli 2012), allows quantification of the con-
646 tributions from different source regions of CAO precipitation, and to disentangle the role different
647 processes play in the water cycle. Thus, novel observational approaches combined with powerful
648 model diagnostics can be invaluable for evaluating and improving the representation of CAOs in
649 models. More fundamentally, they can be a cornerstone for advancing our understanding of the
650 role of CAOs in the high-latitude climate system.

651 *Acknowledgments.* The authors would like to thank Rebecca Guggerli (Université de Fribourg),
652 Stephan Pfahl (FU Berlin), and Fransziska Aemisegger (ETH Zürich) for help with the tagging im-
653 plementation and for helpful discussions, as well as two anonymous reviewers for their thoughtful
654 comments that helped to improve the manuscript. LP acknowledges support by the Swiss National
655 Science Foundation (SNSF), grant P300P2_174307. HS acknowledges support by the Norwegian
656 Research Council (NFR) projects SNOWPACE (grant no. 262710) and ALERTNESS (grant no.
657 280573).

658 **References**

- 659 Azad, R., and A. Sorteberg, 2017: Extreme daily precipitation in coastal western Norway
660 and the link to atmospheric rivers. *J. Geophys. Res. Atmos.*, **122**, 2080–2095, doi:10.1002/
661 2016JD025615.
- 662 Baldauf, M., A. Seifert, J. Förstner, D. Majewski, M. Raschendorfer, and T. Reinhardt, 2011: Op-
663 erational convective-scale numerical weather prediction with the COSMO model: Description
664 and sensitivities. *Mon. Wea. Rev.*, **139**, 3887–3905, doi:10.1175/MWR-D-10-05013.1.
- 665 Bosilovich, M. G., and S. D. Schubert, 2002: Water vapour tracers as diagnostics of the regional
666 hydrologic cycle. *J. Hydrometeorol.*, **3**, 149–165, doi:10.1175/1525-7541(2002)003<0149:
667 WVTADO>2.0.CO;2.
- 668 Bosilovich, M. G., S. D. Schubert, and G. K. Walker, 2005: Global changes of the water cycle
669 intensity. *J. Climate*, **18**, 1591–1608, doi:10.1175/JCLI3357.1.
- 670 Bracegirdle, T. J., and S. L. Gray, 2008: An objective climatology of the dynamical forcing of
671 polar lows in the Nordic seas. *Int. J. Climatol.*, **28**, 1903–1919, doi:10.1002/joc.1686.
- 672 Browning, K. A., 1990: Organization of clouds and precipitation in extratropical cyclones. *Extra-
673 tropical Cyclones. The Erik Palmen Memorial Volume*, C. W. Newton, and E. O. Holopainen,
674 Eds., American Meteorological Society, Boston, USA, 129–153.
- 675 Brümmer, B., 1996: Boundary-layer modification in wintertime cold-air outbreaks from the Arctic
676 sea ice. *Bound.-Layer Meteor.*, **80**, 109–125, doi:10.1007/BF00119014.
- 677 Brümmer, B., 1997: Boundary layer mass, water, and heat budgets in wintertime cold-air out-
678 breaks from the Arctic sea ice. *Mon. Wea. Rev.*, **125**, 1824–1837, doi:10.1175/1520-0493(1997)
679 125\$<\$1824:BLMWAH\$>2.0.CO;2.

- 680 Brümmer, B., 1999: Roll and cell convection in wintertime Arctic cold-air outbreaks. *J. Atmos. Sci.*, **56**, 2613–2636, doi:10.1175/1520-0469(1999)056<2613:RACCIW>2.0.CO;2.
- 682 Brümmer, B., G. Müller, and D. Schröder, 2005: In situ observations in cyclones over Fram Strait. *Meteorol. Z.*, **14**, 721–734, doi:10.1127/0941-2948/2005/0082.
- 684 Bryan, G. H., J. C. Wyngaard, and J. M. Fritsch, 2003: Resolution requirements for the simulation of deep moist convection. *Mon. Wea. Rev.*, **131**, 2394–2416, doi:10.1175/1520-0493(2003)131<2394:RRFTSO>2.0.CO;2.
- 686 Businger, S., and R. J. Reed, 1989: Cyclogenesis in cold air masses. *Weather and Forecasting*, **4**, 133–156.
- 688 Chechin, D. G., C. Lüpkes, I. A. Repina, and V. M. Gryank, 2013: Idealized dry quasi 2-D mesoscale simulations of cold-air outbreaks over the marginal sea ice zone with fine and coarse resolution. *J. Geophys. Res. Atmos.*, **118**, 8787–8813, doi:10.1002/jgrd.50679.
- 690 Cook, P. A., and I. A. Renfrew, 2015: Aircraft-based observations of air-sea turbulent fluxes around the British Isles. *Quart. J. Roy. Meteor. Soc.*, **141**, 139–152, doi:10.1002/qj.2345.
- 692 Dacre, H. F., and S. L. Gray, 2009: The spatial distribution and evolution characteristics of North Atlantic cyclones. *Mon. Wea. Rev.*, **137**, 99–115, doi:10.1175/2008MWR2491.1.
- 694 Dee, D., and Coauthors, 2011: The ERA-Interim reanalysis: configuration and performance of the data assimilation system. *Quart. J. Roy. Meteor. Soc.*, **137**, 553–597, doi:10.1002/qj.828.
- 696 Doms, G., and Coauthors, 2011: A description of the nonhydrostatic regional COSMO model. Part II: Physical parameterization. Tech. rep., Deutscher Wetterdienst, Offenbach, Germany, 154 pp.

- 700 Fairall, C. W., E. F. Bradley, J. E. Hare, A. A. Grachev, and J. B. Edson, 2003: Bulk parameterization of air-sea fluxes: Updates and verification for the COARE algorithm. *J. Climate*, **16**, 571–591, doi:10.1175/1520-0442(2003)016\$(\$0571:BPOASF\$)\$2.0.CO;2.
- 703 Fairall, C. W., E. F. Bradley, D. P. Rogers, J. B. Edson, and G. S. Young, 1996: Bulk parameterization of air-sea fluxes for tropical ocean-global atmosphere coupled-ocean atmosphere response experiment. *J. Geophys. Res.*, **101**, 3747–3764, doi:10.1029/95JC03205.
- 706 Field, P. R., and Coauthors, 2017: Exploring the convective grey zone with regional simulations of a cold air outbreak. *Quart. J. Roy. Meteor. Soc.*, **143**, 2537–2555, doi:10.1002/qj.3105.
- 708 Fletcher, J., S. Mason, and C. Jakob, 2016: The climatology, meteorology, and boundary layer structure of marine cold air outbreaks in both hemispheres. *J. Climate*, **29**, 1999–2014, doi:10.1175/JCLI-D-15-0268.1.
- 711 Grossman, R. L., and A. K. Betts, 1990: Air-sea interaction during an extreme cold air outbreak from the eastern coast of the United States. *Mon. Wea. Rev.*, **118**, 324–342, doi:10.1175/1520-0493(1990)118\$(\$0324:AIDAEC\$)\$2.0.CO;2.
- 714 Gryschka, M., J. Fricke, and S. Raasch, 2014: On the impact of forced roll convection on vertical turbulent transport in cold air outbreaks. *J. Geophys. Res. Atmos.*, **119**, 12 513–12 532, doi:10.1002/2014JD022160.
- 717 Harden, B. E., I. A. Renfrew, and G. N. Petersen, 2015: Meteorological buoy observations from the central Iceland Sea. *J. Geophys. Res. Atmos.*, **120**, 3199–3208, doi:10.1002/2014JD022584.
- 719 Hartmann, J., C. Kottmeier, and S. Raasch, 1997: Roll vortices and boundary-layer development during a cold air outbreak. *Bound.-Layer Meteor.*, **84**, 45–65, doi:10.1023/A:1000392931768.

- 721 Hoskins, B. J., M. E. McIntyre, and A. W. Robertson, 1985: On the use and significance of
722 isentropic potential vorticity maps. *Quart. J. Roy. Meteor. Soc.*, **111**, 877–946, doi:10.1002/qj.
723 49711147002.
- 724 Iwasaki, T., T. Shoji, Y. Kanno, M. Sawada, M. Ujiie, and K. Takaya, 2014: Isentropic analysis of
725 polar cold airmass streams in the Northern Hemispheric winter. *J. Atmos. Sci.*, **71**, 2230–2243,
726 doi:10.1175/JAS-D-13-058.1.
- 727 Jahnke-Bornemann, A., and B. Brümmer, 2009: The Iceland-Lofotes pressure difference: different
728 states of the North Atlantic low-pressure zone. *Tellus A*, **61**, 466–475, doi:10.1111/j.1600-0870.
729 2009.00401.x.
- 730 Joussaume, S., R. Sadourny, and J. Jouzel, 1984: A general circulation model of water isotope
731 cycles in the atmosphere. *Nature*, **311**, 24–29, doi:10.1038/311024a0.
- 732 Kew, S. F., M. Sprenger, and H. C. Davies, 2010: Potential vorticity anomalies of the low-
733 ermost stratosphere: A 10-yr winter climatology. *Mon. Wea. Rev.*, **138**, 1234–1249, doi:
734 10.1175/2009MWR3193.1.
- 735 Kolstad, E. W., 2011: A global climatology of favourable conditions for polar lows. *Quart. J. Roy.*
736 *Meteor. Soc.*, **137**, 1749–1761, doi:10.1002/qj.888.
- 737 Kolstad, E. W., 2017: Higher ocean wind speeds during marine cold air outbreaks. *Quart. J. Roy.*
738 *Meteor. Soc.*, **143**, 2084–2092, doi:10.1002/qj.3068.
- 739 Kolstad, E. W., T. J. Bracegirdle, and I. A. Seierstad, 2009: Marine cold-air outbreaks in the North
740 Atlantic: temporal distribution and associations with large-scale atmospheric circulation. *Clim.*
741 *Dyn.*, **33**, 187–197, doi:10.1007/s00382-008-0431-5.

- 742 Koster, R., J. Jouzel, R. Souzzo, G. Russell, W. Broecker, D. Rind, and P. Eagleson, 1986: Global
743 sources of local precipitation as determined by the NASA/GISS GCM. *Geophys. Res. Lett.*, **13**,
744 121–124, doi:10.1029/GL013i002p00121.
- 745 Kristovich, D. A. R., and Coauthors, 2000: The lake-induced convection experiment and the snow-
746 band dynamics project. *Bull. Am. Meteorol. Soc.*, **81**, 519–542, doi:10.1175/1520-0477(2000)
747 081⟨0519:TLCEAT⟩2.3.CO;2.
- 748 Laederach, A., and H. Sodemann, 2016: A revised picture of the atmospheric moisture residence
749 time. *Geophys. Res. Lett.*, **43**, 924 – 933, doi:10.1002/2015GL067449.
- 750 Louis, J., 1979: A parametric model of vertical eddy fluxes in the atmosphere. *Bound.-Layer*
751 *Meteor.*, **17**, 187–202.
- 752 Lüpkes, C., and K. H. Schlünzen, 1996: Modelling the Arctic convective boundary-layer
753 with different turbulence parameterizations. *Bound.-Layer Meteor.*, **79**, 107–130, doi:10.1007/
754 BF00120077.
- 755 Madonna, E., H. Wernli, and H. Joos, 2014: Warm conveyor belts in the ERA-Interim dataset
756 (1979–2010). Part I: Climatology and potential vorticity evolution. *J. Climate*, **27**, 3–26, doi:
757 10.1175/JCLI-D-12-00720.1.
- 758 Marshall, J., and F. Schott, 1999: Open-ocean convection: Observations, theory, and models. *Rev.*
759 *Geophys.*, **37**, 1–64, doi:10.1029/98rg02739.
- 760 Numaguti, A., 1999: Origin and recycling processes of precipitating water over the Eurasian
761 continent: Experiments using an atmospheric general circulation model. *J. Geophys. Res.*, **104**,
762 1957–1972, doi:10.1029/1998JD200026.

- 763 Pagowski, M., and G. W. K. Moore, 2001: A numerical study of an extreme cold-air outbreak over
764 the Labrador Sea: Sea ice, air-sea interaction, and development of polar lows. *Mon. Wea. Rev.*,
765 **129**, 47–72, doi:10.1175/1520-0493(2001)129\$(\$0047:ANSOAE\$)\$2.0.CO;2.
- 766 Papritz, L., and C. Grams, 2018: Linking low-frequency large-scale circulation patterns to cold
767 air outbreak formation in the north-eastern North Atlantic. *Geophys. Res. Lett.*, **45**, 2542–2553,
768 doi:10.1002/2017GL076921.
- 769 Papritz, L., and S. Pfahl, 2016: Importance of latent heating in mesocyclones for the decay of cold
770 air outbreaks: A numerical process study from the Pacific sector of the Southern Ocean. *Mon.*
771 *Wea. Rev.*, **144**, 315–336, doi:10.1175/MWR-D-15-0268.1.
- 772 Papritz, L., S. Pfahl, H. Sodemann, and H. Wernli, 2015: A climatology of cold air outbreaks and
773 their impact on air-sea heat fluxes in the high-latitude South Pacific. *J. Climate*, **28**, 342–364,
774 doi:10.1175/JCLI-D-14-00482.1.
- 775 Papritz, L., and T. Spengler, 2017: A Lagrangian climatology of wintertime cold air outbreaks
776 in the Irminger and Nordic seas and their role in shaping air-sea heat fluxes. *J. Climate*, **30**,
777 2717–2737, doi:10.1175/JCLI-D-16-0605.1.
- 778 Pfahl, S., E. Madonna, M. Boettcher, H. Joos, and H. Wernli, 2014: Warm conveyor belts in the
779 ERA-Interim dataset (1979–2010). Part II: Moisture origin and relevance for precipitation. *J.*
780 *Climate*, **27**, 27–40, doi:10.1175/JCLI-D-13-00223.1.
- 781 Pfahl, S., and H. Sodemann, 2014: What controls deuterium excess in global precipitation? *Clim.*
782 *Past*, **10**, 771–781, doi:10.5194/cp-10-771-2014.
- 783 Pfahl, S., and H. Wernli, 2012: Quantifying the relevance of cyclones for precipitation extremes.
784 *J. Climate*, **25**, 6770–6780, doi:10.1175/JCLI-D-11-00705.1.

- 785 Pfahl, S., H. Wernli, and K. Yoshimura, 2012: The isotopic composition of precipitation from a
786 winter storm - a case study with the limited-area model comsmoiso. *Atmos. Chem. Phys.*, **12**,
787 1629–1648, doi:10.5194/acp-12-1629-2012.
- 788 Rasmussen, E., and J. Turner, 2003: *Polar Lows: Mesoscale Weather Systems in the Polar Regions*.
789 Cambridge University Press, Cambridge, U.K., 612 pp.
- 790 Renfrew, I. A., and G. W. K. Moore, 1999: An extreme cold-air outbreak over the Labrador
791 Sea: Roll vortices and air-sea interaction. *Mon. Wea. Rev.*, **127**, 2379–2394, doi:10.1175/1520-0493(1999)127\$2379:AECAOO\$2.0.CO;2.
- 793 Schröder, D., G. Heinemann, and S. Willmes, 2011: The impact of a thermodynamic sea-ice
794 module in the COSMO numerical weather prediction model on simulations for the Laptev Sea,
795 Siberian Arctic. *Polar Research*, **30**, 6334, doi:10.3402/polar.v30i0.6334.
- 796 Segtnan, O. H., T. Furevik, and A. D. Jenkins, 2011: Heat and freshwater budgets of the Nordic
797 seas computed from atmospheric reanalysis and ocean observations. *J. Geophys. Res.*, **116**,
798 C11 003, doi:10.1029/2011JC006939.
- 799 Shapiro, M. A., L. S. Fedor, and T. Hampel, 1987: Research aircraft measurements of a polar low
800 over the Norwegian Sea. *Tellus*, **39A**, 272–306, doi:10.1111/j.1600-0870.1987.tb00309.x.
- 801 Skillingstad, E. D., and J. B. Edson, 2009: Large-eddy simulation of moist convection dur-
802 ing a cold air outbreak over the Gulf Stream. *J. Atmos. Sci.*, **66**, 1274–1293, doi:10.1175/2008JAS2755.1.
- 804 Sodemann, H., and A. Stohl, 2013: Moisture origin and meridional transport in atmospheric rivers,
805 and their association with multiple cyclones. *Mon. Wea. Rev.*, **141**, 2850 – 2868, doi:10.1175/MWR-D-12-00256.1.

- 807 Sodemann, H., H. Wernli, and C. Schwierz, 2009: Sources of water vapour contributing to the
808 elbe flood in august 2002 - a tagging study in a mesoscale model. *Quart. J. Roy. Meteor. Soc.*,
809 **135**, 205–223, doi:10.1002/qj.374.
- 810 Spensberger, C., and M. Sprenger, 2017: Beyond cold and warm: An objective classification for
811 maritime mid-latitude fronts. *Quart. J. Roy. Meteor. Soc.*, doi:10.1002/qj.3199, in press.
- 812 Steen-Larsen, H. C., and Coauthors, 2015: Moisture sources and synoptic to seasonal variability
813 of north atlantic water vapor isotopic composition. *J. Geophys. Res. Atmos.*, **120**, 5757–5774,
814 doi:10.1002/2015JD023234.
- 815 Steppeler, J., G. Doms, U. Schättler, H. W. Bitzer, A. Gassmann, U. Damrath, and G. Gregoric,
816 2003: Meso-gamma scale forecasts using the nonhydrostatic model LM. *Meteor. Atmos. Phys.*,
817 **82**, 75–96, doi:10.1007/s00703-001-0592-9.
- 818 Stohl, A., C. Forster, and H. Sodemann, 2008: Remote sources of water vapor forming precipi-
819 tation on the norwegian west coast at 60°n - a tale of hurricanes and an atmospheric river. *J.*
820 *Geophys. Res.*, **113**, D05 102, doi:10.1029/2007JD009006.
- 821 Terpstra, A., T. Spengler, and R. W. Moore, 2015: Idealised simulations of polar low development
822 in an Arctic moist-baroclinic environment. *Quart. J. Roy. Meteor. Soc.*, doi:10.1002/qj.2507,
823 accepted.
- 824 Tiedtke, M., 1989: A comprehensive mass flux scheme for cumulus parameterization in large-scale
825 models. *Mon. Wea. Rev.*, **117**, 1779–1800, doi:10.1175/1520-0493(1989)117,1779:ACMFSF.2.
826 0.CO;2.
- 827 Tomassini, L., P. R. Field, R. Honnert, S. Malardel, R. McTaggart-Cowan, K. Saitou, A. T. Noda,
828 and A. Seifert, 2017: The “grey zone” cold air outbreak global model intercomparison: A cross

- 829 evaluation using large-eddy simulations. *J. Adv. Model. Earth Syst.*, **9**, 39–64, doi:10.1002/
- 830 2016MS000822.
- 831 Škerlak, B., M. Sprenger, S. Pfahl, E. Tyrllis, and H. Wernli, 2015: Tropopause folds in ERA-
- 832 Interim: Global climatology and relation to extreme weather events. *J. Geophys. Res. Atmos.*,
- 833 **120**, 4860–4877, doi:10.1002/2014JD022787.
- 834 Vannière, B., A. Czaja, H. Dacre, T. Woollings, and R. Parfitt, 2016: A potential vorticity signature
- 835 for the cold sector of winter extratropical cyclones. *Quart. J. Roy. Meteor. Soc.*, **142**, 432–442,
- 836 doi:10.1111/qj.1600-0870.2010.00492.x.
- 837 Vihma, T., and B. Brümmer, 2002: Observations and modelling of the on-ice and off-ice
- 838 air flow over the Northern Baltic Sea. *Bound.-Layer Meteor.*, **103**, 1–27, doi:10.1023/A:
- 839 1014566530774.
- 840 Wacker, U., K. V. Jayaraman Potty, C. Lüpkes, J. Hartmann, and M. Raschendorfer, 2005: A case
- 841 study on a polar cold air outbreak over Fram Strait using a mesoscale weather prediction model.
- 842 *Bound.-Layer Meteor.*, **117**, 301–336, doi:10.1007/s10546-005-2189-1.
- 843 Wang, Y., B. Geerts, and Y. Chen, 2016: Vertical structure of boundary layer convection during
- 844 cold-air outbreaks at Barrow, Alaska. *J. Geophys. Res. Atmos.*, **121**, 399–412, doi:10.1002/
- 845 2015JD023506.
- 846 Wernli, H., and C. Schwierz, 2006: Surface cyclones in the ERA-40 dataset (1958–2001). Part
- 847 I: Novel identification method and global climatology. *J. Atmos. Sci.*, **63**, 2486–2507, doi:10.
- 848 1175/JAS3766.1.

- 849 Winschall, A., S. Pfahl, H. Sodemann, and H. Wernli, 2012: Impact of north atlantic evaporation
- 850 hot spots on southern Alpine heavy precipitation events. *Quart. J. Roy. Meteor. Soc.*, **138**, 1245–
- 851 1258, doi:10.1002/qj.987.
- 852 Winschall, A., S. Pfahl, H. Sodemann, and H. Wernli, 2014: Comparison of Eulerian and La-
- 853 grangian moisture source diagnostics – the flood event in eastern Europe in May 2010. *Atmos.*
- 854 *Chem. Phys.*, **14**, 6605–6619, doi:10.5194/acp-14-6605-2014.

855 **LIST OF TABLES**

856	Table 1. Model configurations for the five simulations. The COSMO 0.02° simulations	40
857	are run in the nested domain, while the other simulations are run on the full	
858	domain (compare Fig. 1a). The grid size denotes the dimensions of the grid in	
859	the zonal, meridional and vertical direction, respectively.	
860	Table 2. Accumulated marine CAO precipitation area integrated over the Greenland,	41
861	Iceland and Norwegian Seas (cf. GIN box Fig. 1a) for all CAO tracers, and	
862	separately for the two tracers released between 48 - 60 h and 60 - 72 h, respec-	
863	tively, for simulations at $0.2^\circ \times 0.2^\circ$ to $0.05^\circ \times 0.05^\circ$ resolution. The period of	
864	accumulation is 1800 UTC 23 Dec until 0000 UTC 27 Dec and the contribu-	
865	tions are separated into grid-scale and convective precipitation. The integrated	
866	precipitation is expressed in units of 10^{12} kg.	

867 TABLE 1. Model configurations for the five simulations. The COSMO 0.02° simulations are run in the nested
 868 domain, while the other simulations are run on the full domain (compare Fig. 1a). The grid size denotes the
 869 dimensions of the grid in the zonal, meridional and vertical direction, respectively.

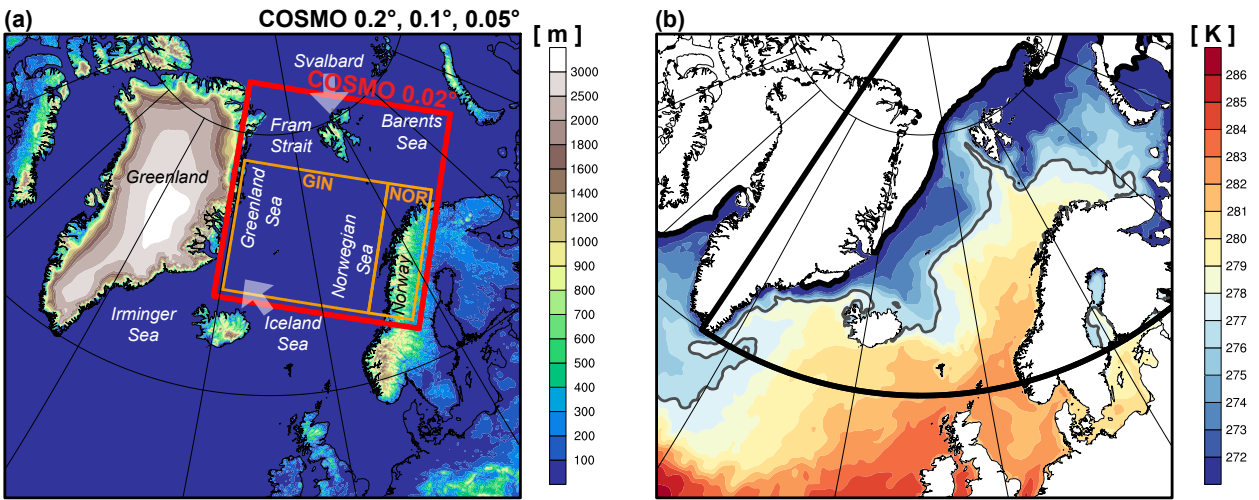
name	horizontal grid-spacing	grid size	initialization time	duration	convection scheme
COSMO 0.2°	$0.2^\circ \times 0.2^\circ$	$200 \times 180 \times 40$	1200 UTC 23 Dec	144 h	Tiedtke (1989)
COSMO 0.1°	$0.1^\circ \times 0.1^\circ$	$400 \times 360 \times 60$	1200 UTC 23 Dec	144 h	Tiedtke (1989)
COSMO 0.05°	$0.05^\circ \times 0.05^\circ$	$800 \times 720 \times 60$	1200 UTC 23 Dec	144 h	Tiedtke (1989)
COSMO 0.02° nc	$0.02^\circ \times 0.02^\circ$	$800 \times 840 \times 60$	1500 UTC 23 Dec	81 h	none
COSMO 0.02° sc	$0.02^\circ \times 0.02^\circ$	$800 \times 840 \times 60$	1500 UTC 23 Dec	81 h	reduced Tiedtke (1989) (shallow)

870 TABLE 2. Accumulated marine CAO precipitation area integrated over the Greenland, Iceland and Norwegian
 871 Seas (cf. GIN box Fig. 1a) for all CAO tracers, and separately for the two tracers released between 48 - 60 h and
 872 60 - 72 h, respectively, for simulations at $0.2^\circ \times 0.2^\circ$ to $0.05^\circ \times 0.05^\circ$ resolution. The period of accumulation
 873 is 1800 UTC 23 Dec until 0000 UTC 27 Dec and the contributions are separated into grid-scale and convective
 874 precipitation. The integrated precipitation is expressed in units of 10^{12} kg.

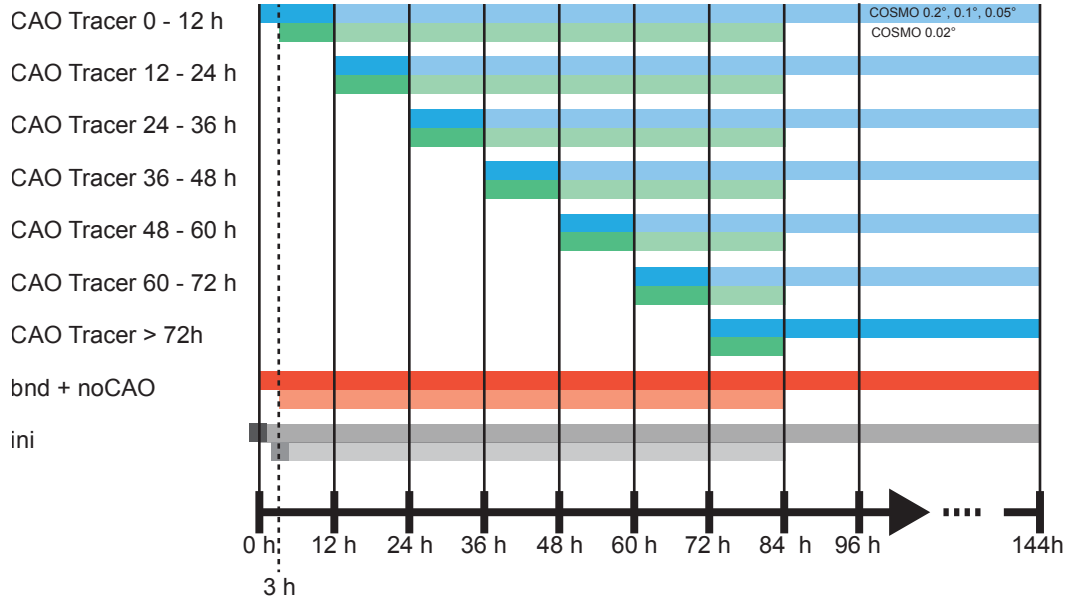
		$0.2^\circ \times 0.2^\circ$	$0.1^\circ \times 0.1^\circ$	$0.05^\circ \times 0.05^\circ$
CAO all tracers	grid-scale	7.62	7.58	6.86
	convective	0.80	1.36	2.53
CAO tracer 48 - 60 h	grid-scale	1.83	1.81	1.51
	convective	0.27	0.55	0.98
CAO tracer 60 - 72 h	grid-scale	1.44	1.46	1.26
	convective	0.23	0.44	0.92

875 **LIST OF FIGURES**

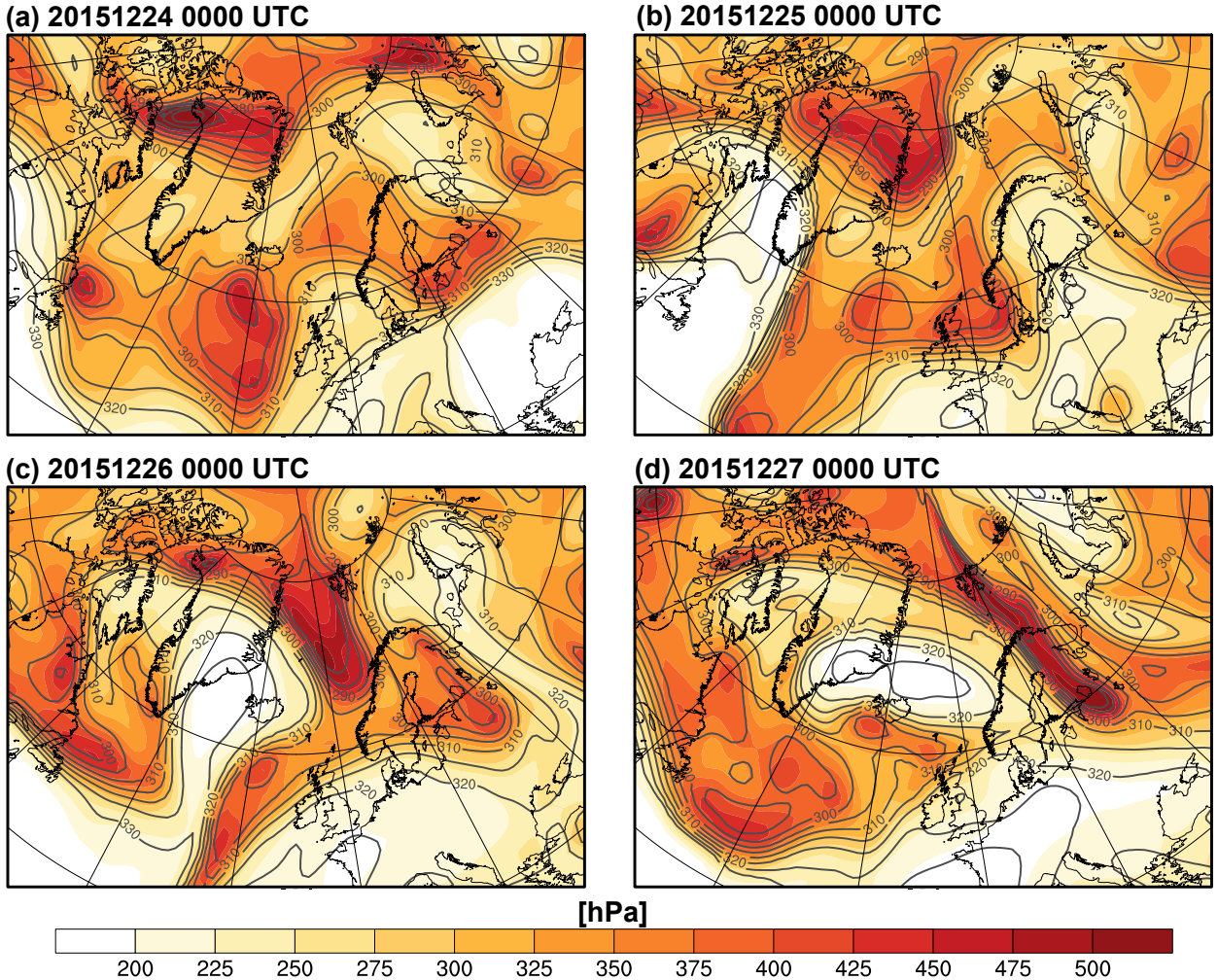
968 and with (sc) shallow convection scheme active. The accumulation is from 1800 UTC 23
969 Dec (+6 h) until 0000 UTC 27 Dec (+84 h). Contributions are shown separately for initial
970 vapor (light gray), vapor entering the domain from the boundary or the surface outside of
971 the CAO mask (dark gray), and vapor of CAO origin released in 12-hourly intervals (color). . . 58



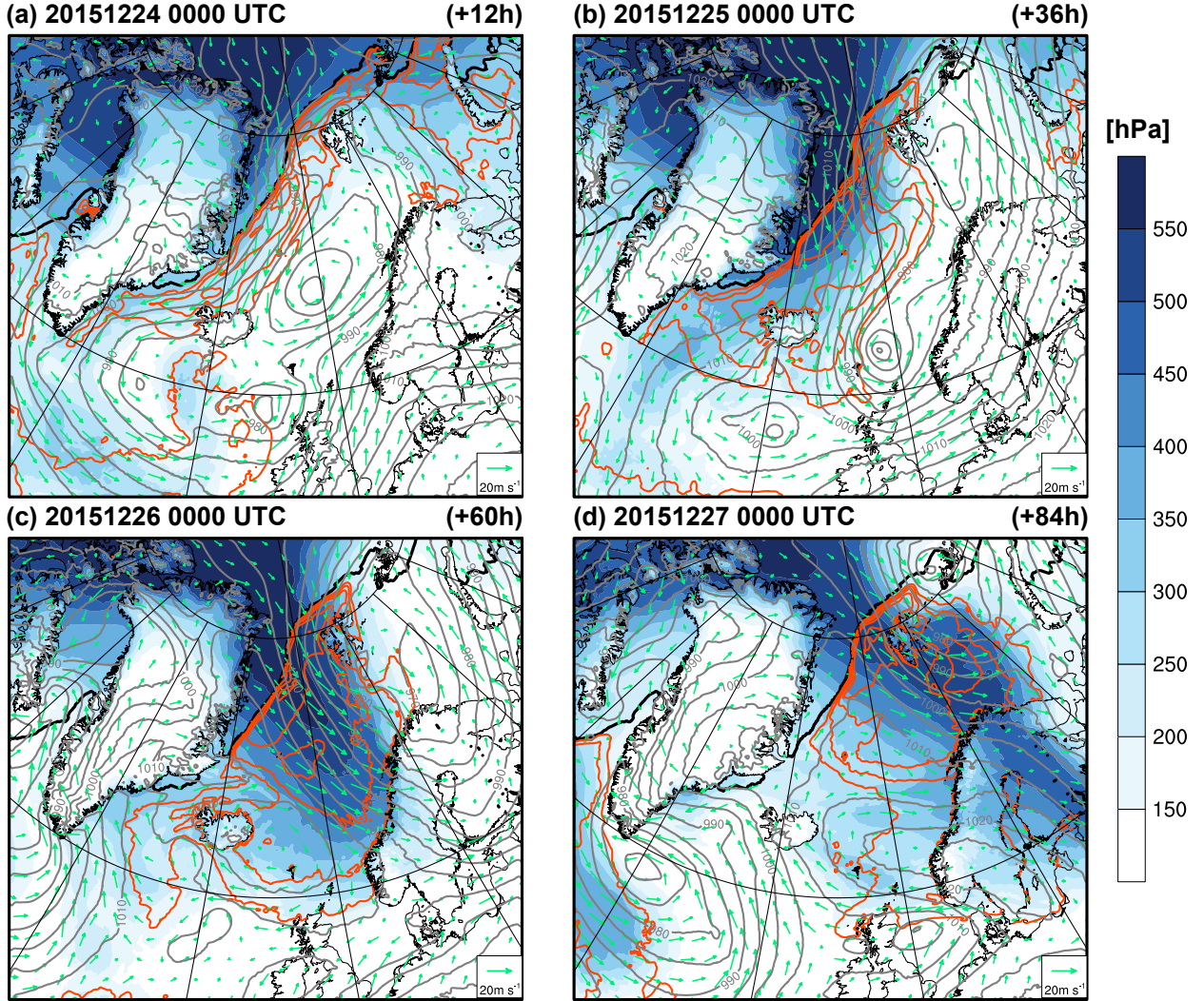
972 FIG. 1. (a) Domain of the COSMO 0.2° , 0.1° , 0.05° simulations and the nested domain of the COSMO 0.02°
 973 simulations (red frame). The shading indicates model topography in the COSMO 0.05° simulation. Furthermore,
 974 the regions over which precipitation is integrated are indicated by the orange boxes (GIN and NOR boxes) and
 975 key locations are marked. (b) Sea surface temperature (shading) with the location of the Arctic front highlighted
 976 by the 277 K isotherm (gray line) and the sea ice edge (thick black). The black box outlines the region in which
 977 evaporation into the CAO air mass is tagged.



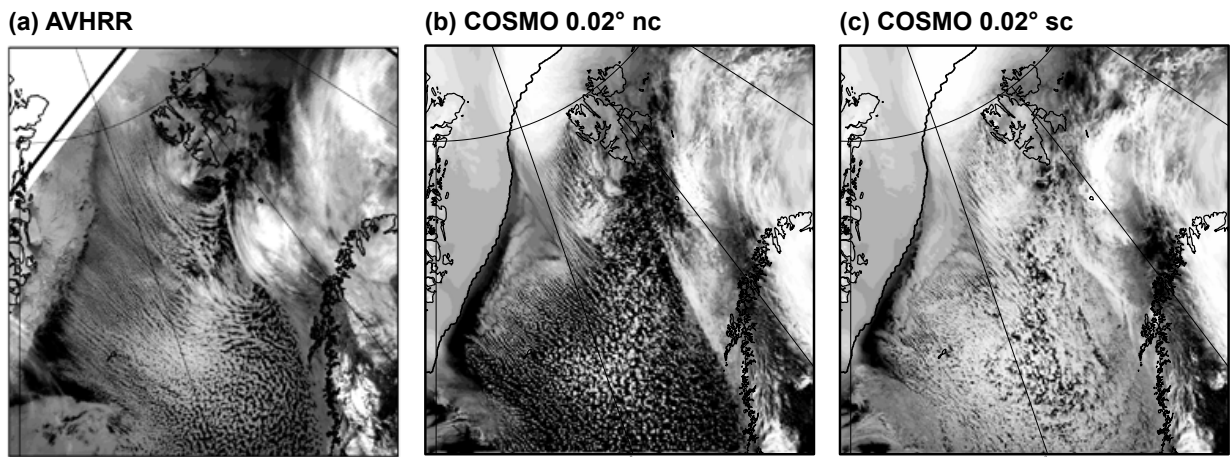
978 FIG. 2. Temporal definition of the tracers. Blue and green stand for CAO tracers where strong (weak) colors
 979 indicate the time window during which the tracer is released (carried through the model integration but no longer
 980 released), red for the tracer representing water entering the domain by advection across the domain boundaries
 981 and by evaporation into non-CAO air masses, and gray for the tracer representing water initially present in the
 982 domain. The dashed vertical line indicates the initialization time of the $0.02^\circ \times 0.02^\circ$ simulations. The upper and
 983 lower horizontal bars refer to the definition of the tracers in the COSMO 0.2° , 0.1° , 0.05° and COSMO 0.02°
 984 simulations, respectively, which have different initialization and forecast lead times (cf. Table 1).



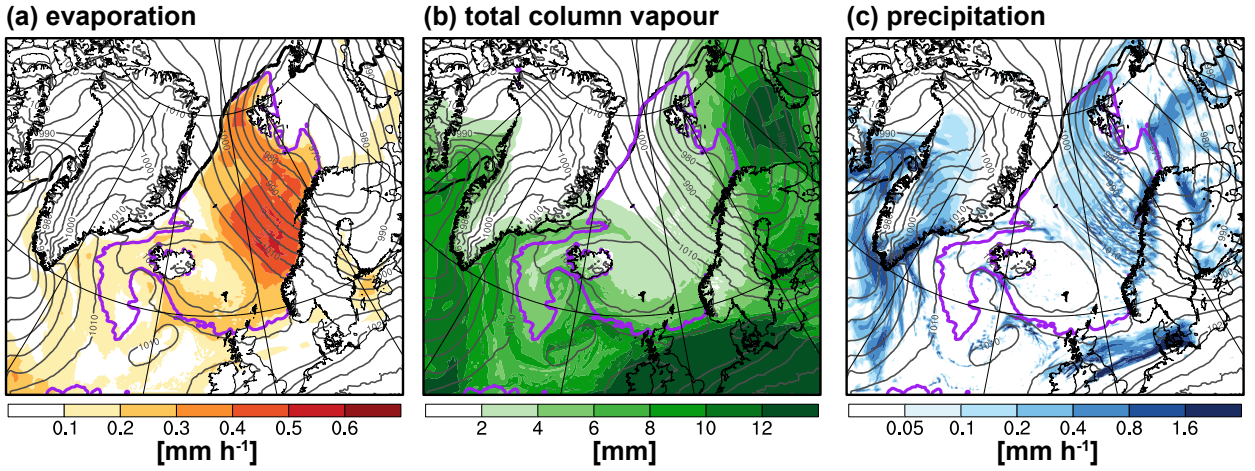
985 FIG. 3. Temporal evolution of pressure (shading) and potential temperature (gray, contour interval 5 K) at the
986 dynamical tropopause from (a) 0000 UTC 24 Dec to (d) 0000 UTC 27 Dec in daily intervals. Data is from the
987 ERA-Interim reanalysis (Dee et al. 2011). The dynamical tropopause is defined as the 2 pvu potential vorticity
988 iso-surface ($1 \text{ pvu} = 10^{-6} \text{ Km}^2 \text{kg}^{-1} \text{s}^{-1}$; cf. Hoskins et al. 1985; Škerlak et al. 2015).



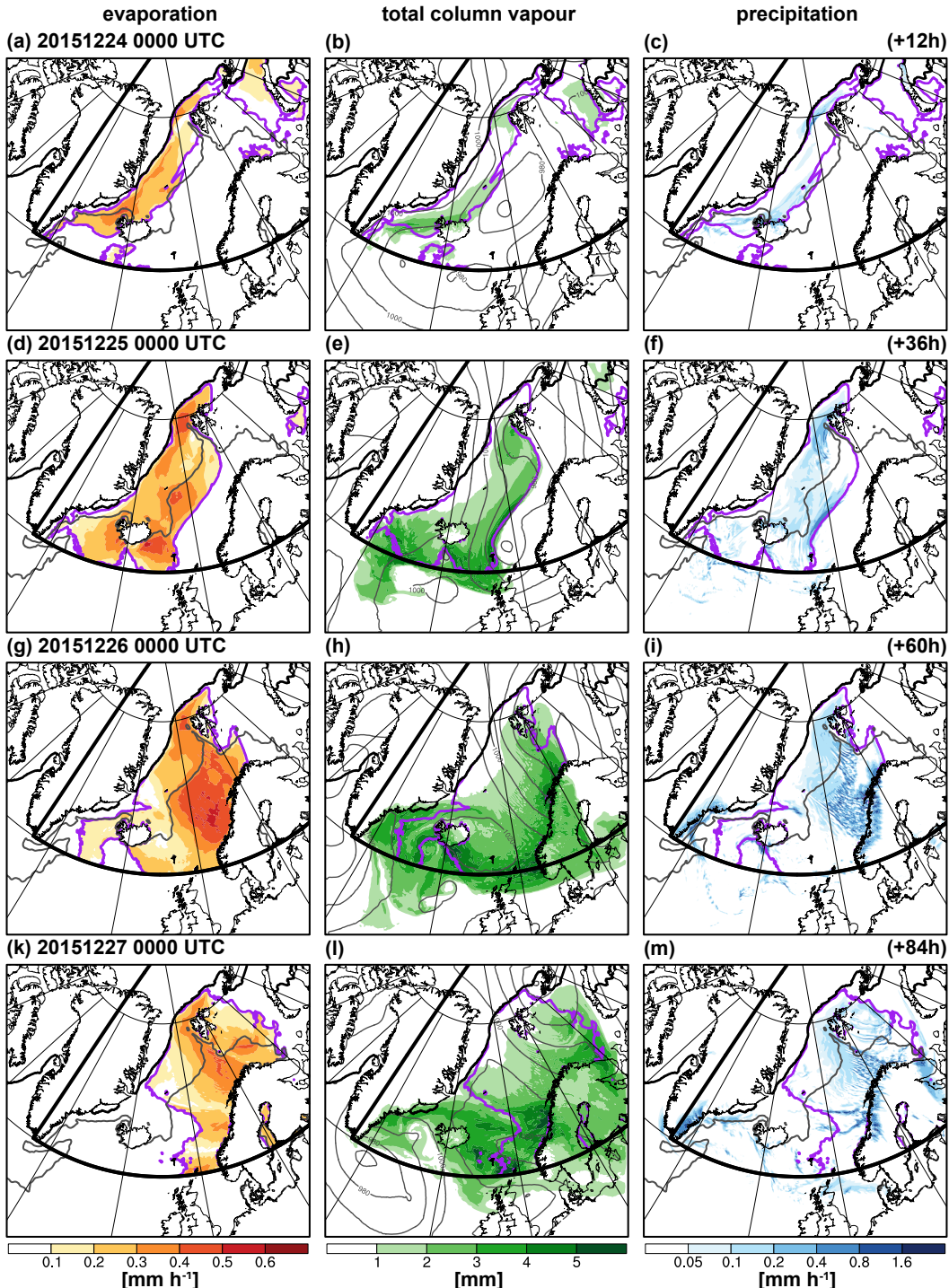
989 FIG. 4. Synoptic evolution of the cold air outbreak from (a) 0000 UTC 24 Dec to (d) 0000 UTC 27 Dec in
 990 daily intervals. Shown are cold air mass (mass below 280 K isentropic surface in hPa; shading), CAO index
 991 ($\theta_{SST} - \theta_{900}$; red, contours from 4 K in intervals of 4 K), sea level pressure (gray, contours in intervals of 5 hPa),
 992 winds on lowest model level (~ 10 m above ground, green arrows), and the sea ice edge (thick black). Data is
 993 from the COSMO 0.05° simulation.



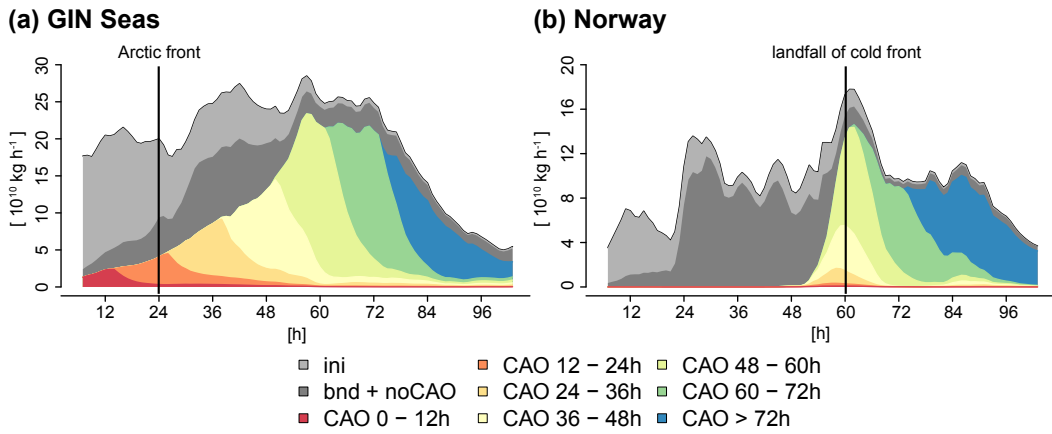
994 FIG. 5. (a) Infrared (channel 4) satellite image from the NOAA-17 AVHRR instrument valid at 1935 UTC 25
995 Dec 2015. (b, c) Top of the atmosphere outgoing longwave radiation in the COSMO $0.02^\circ \times 0.02^\circ$ simulation
996 without (nc, b) and with (sc, c) shallow convection parameterization at 1900 UTC 25 Dec 2015.



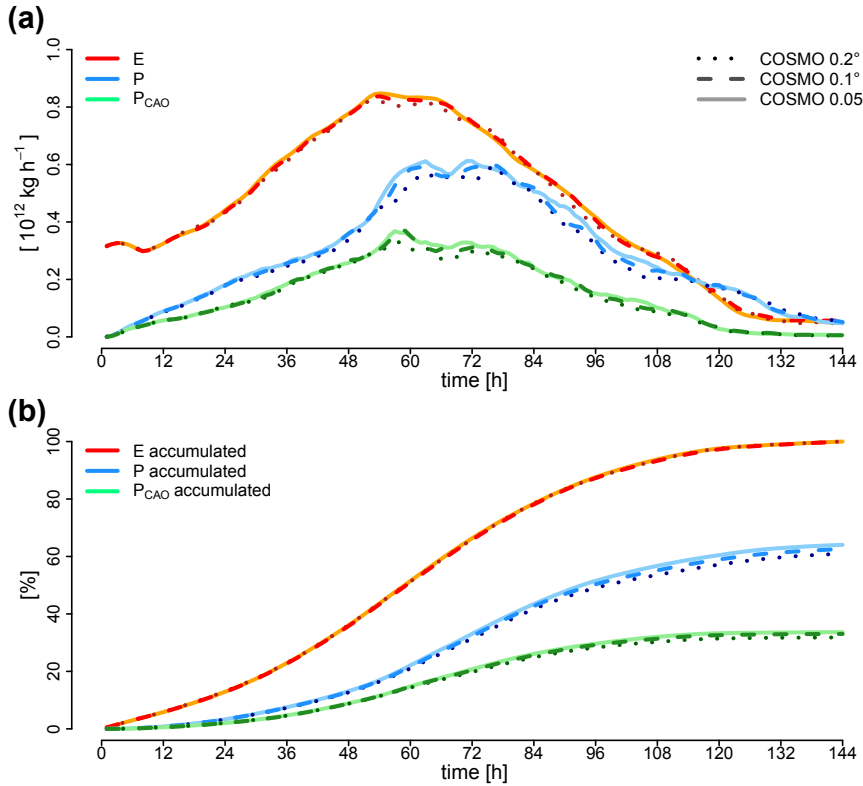
997 FIG. 6. Snapshots of (a) evaporation from the ocean surface, (b) total column vapor, and (c) precipitation at
998 0000 UTC 26 Dec (+60 h). Evaporation and precipitation are averaged over the previous hour. Further shown
999 are sea level pressure (gray, contour interval 5 K), the 4 K isoline of the CAO index ($\theta_{\text{SST}} - \theta_{900}$; purple), and
1000 the sea ice edge (thick black). Data is from the COSMO 0.05° simulation.



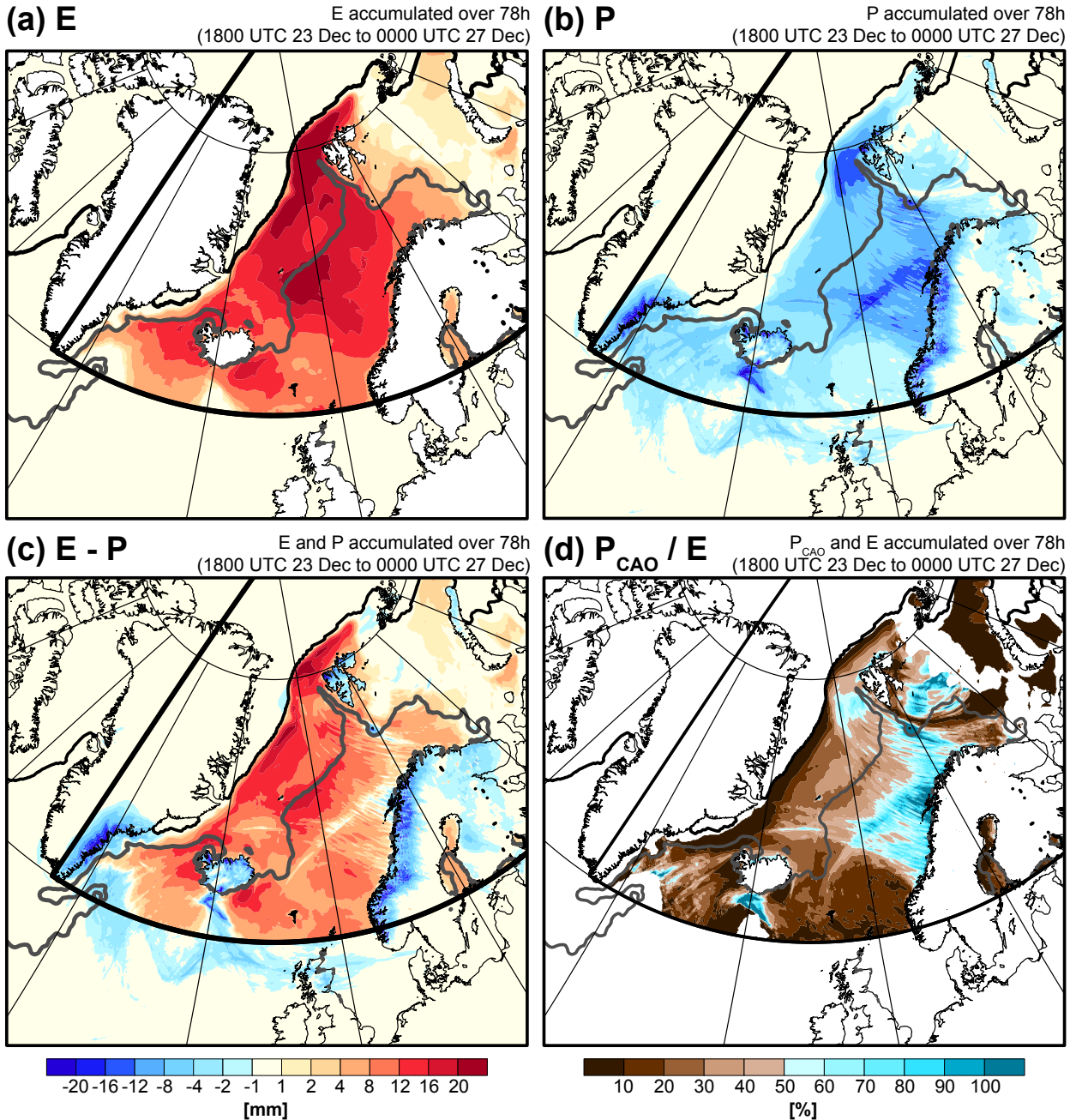
1001 FIG. 7. Snapshots of tagged evaporation into the CAO air mass (left column)
1002 (middle column), and tagged CAO column vapor (right column) at (a-c) 0000 UTC 24 Dec, (d-f) 0000 UTC 25
1003 Dec, (g-i) 0000 UTC 26 Dec, and (k-m) 0000 UTC 27 Dec. Evaporation and precipitation are averages over the
1004 previous hour. Note that evaporation into the CAO air mass is tagged only poleward of 60°N and east of 45°W
1005 (cf. thick black lines). Further shown are the CAO evaporation region (purple) and the sea ice edge (black), as
1006 well as sea level pressure (middle column; gray contours in intervals of 10 hPa; omitted over land) and the 277 K
1007 isotherm of SST with cold waters located to the left and north of the isoline (left and right columns; gray line).



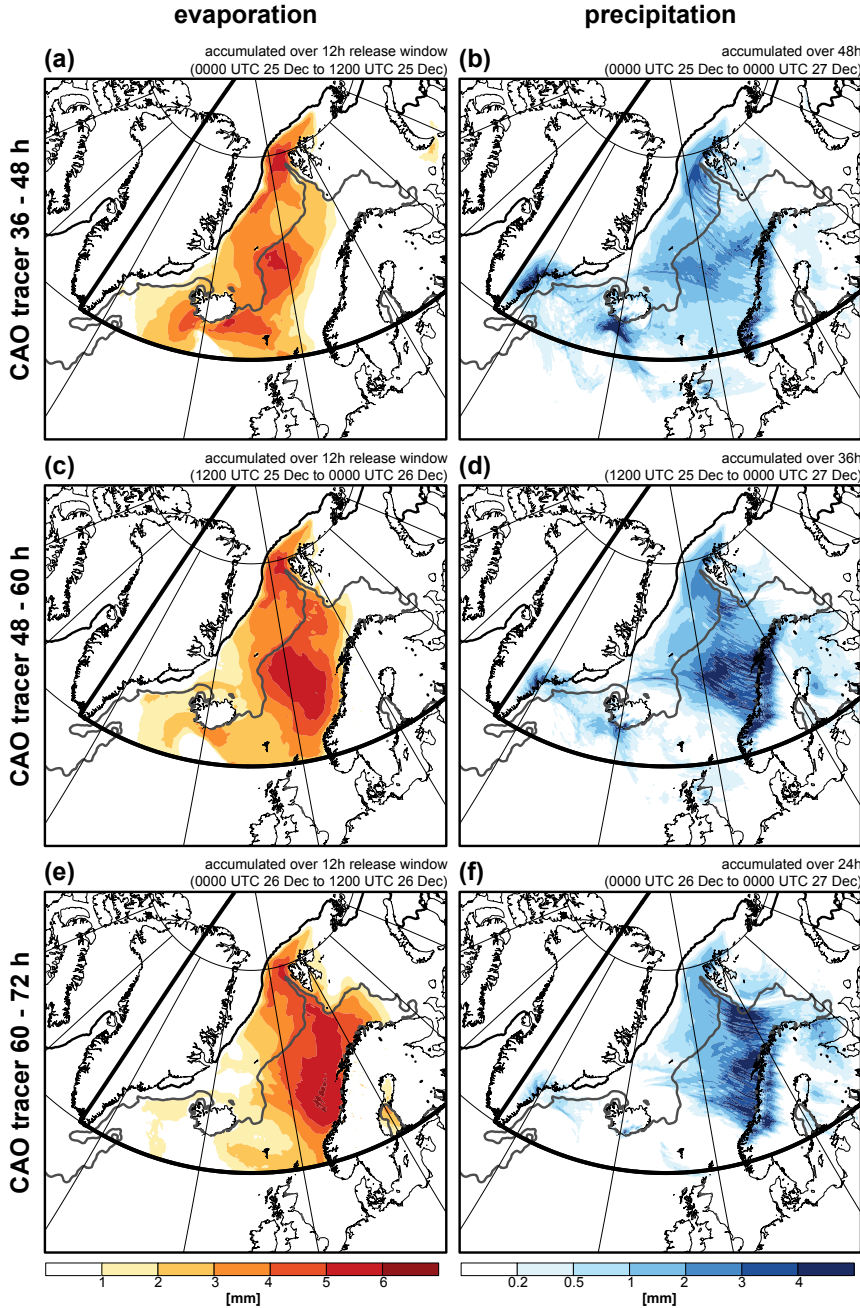
1009 FIG. 8. Temporal evolution of tagged precipitation integrated over (a) the Greenland, Iceland and Norwegian
 1010 Seas (GIN box, Fig. 1a) and (b) Norway (NOR box, Fig. 1a) with contributions shown separately for tagged
 1011 vapor initially present in the domain (light gray), entering the domain from the boundary or the surface outside
 1012 of the CAO mask (dark gray), and associated with the CAO tracers that are released in 12-hourly intervals
 1013 (color). Time axis is relative to the initial time of the simulation and the time when the CAO air mass reaches
 1014 across the Arctic front and the cold front makes landfall are indicated in (a) and (b), respectively. Data is from
 1015 the COSMO 0.05° simulation.



1016 FIG. 9. Temporal evolution of domain integrated tagged CAO water budget. (a) Rates of tagged evaporation
 1017 into the CAO air mass (red), tagged CAO precipitation (blue), and tagged CAO precipitation collocated with the
 1018 CAO mask ($\theta_{SST} - \theta_{900} = 4 \text{ K}$; green). (b) Same as in (a) but accumulated over time and expressed in % of the
 1019 total evaporation into the CAO air mass over the whole length of the simulation. All quantities are shown for the
 1020 COSMO 0.2° (dotted), COSMO 0.1° (dashed), and COSMO 0.05° (solid) simulations.

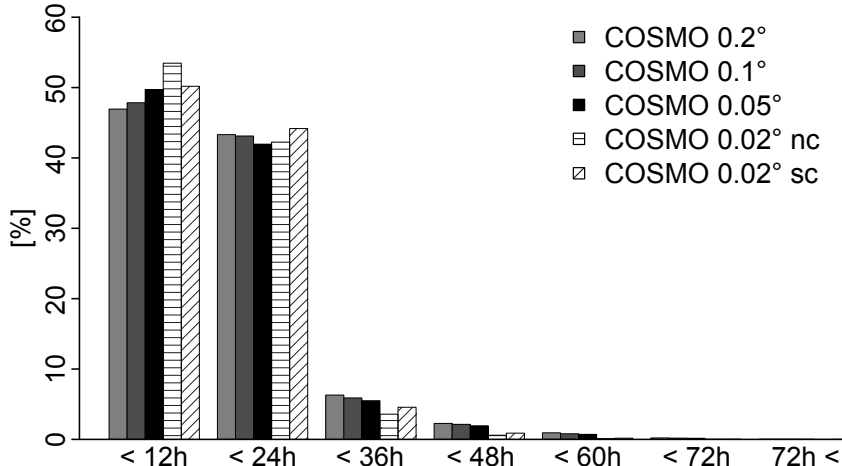


1021 FIG. 10. Footprints of tagged CAO (a) evaporation, (b) precipitation, (c) evaporation minus precipitation, and
 1022 (d) the ratio of precipitation collocated with the CAO evaporation mask ($\theta_{\text{SST}} - \theta_{900} = 4K$) and evaporation in
 1023 %. Evaporation and precipitation are accumulated over 78 h in the interval from 1800 UTC 23 Dec (+6 h) to
 1024 0000 UTC 27 Dec (+84 h). Note that the scale in (c) applies also to (a) and (b) to facilitate comparison. Regions
 1025 with evaporation of less than 1 mm are masked out in (d). Furthermore, the 277 K isotherm of SST is drawn to
 1026 illustrate the location of the Arctic front (gray line). Cold waters are located to the west and north of this line.
 1027 Data is from the COSMO 0.05° simulation.

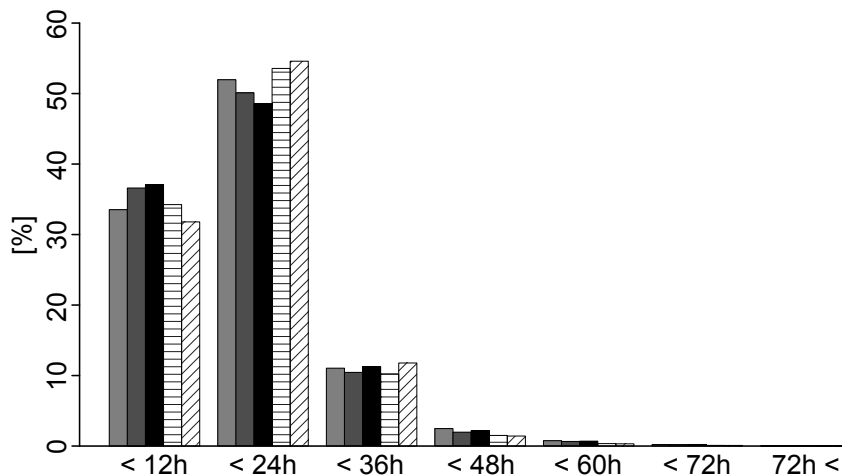


1028 FIG. 11. Footprints of tagged CAO evaporation (left column) and precipitation (right column) for tracers
 1029 released between (a, b) 0000 UTC 25 Dec and 1200 UTC 25 Dec (36 to 48 h), (c, d) 1200 UTC 25 Dec and 0000
 1030 UTC 26 Dec (48 to 60 h), and (e, f) 0000 UTC 26 Dec and 1200 UTC 26 Dec (60 to 72 h) in the $0.05^\circ \times 0.05^\circ$
 1031 simulation. Evaporation is accumulated over the respective release window of each tracer, and precipitation is
 1032 accumulated from the start of the release window until 0000 UTC 27 Dec. The 277 K isotherm of SST is drawn
 1033 to illustrate the location of the Arctic front (gray line). Cold waters are located to the west and north of this line.
 1034 Data is from the COSMO 0.05° simulation.

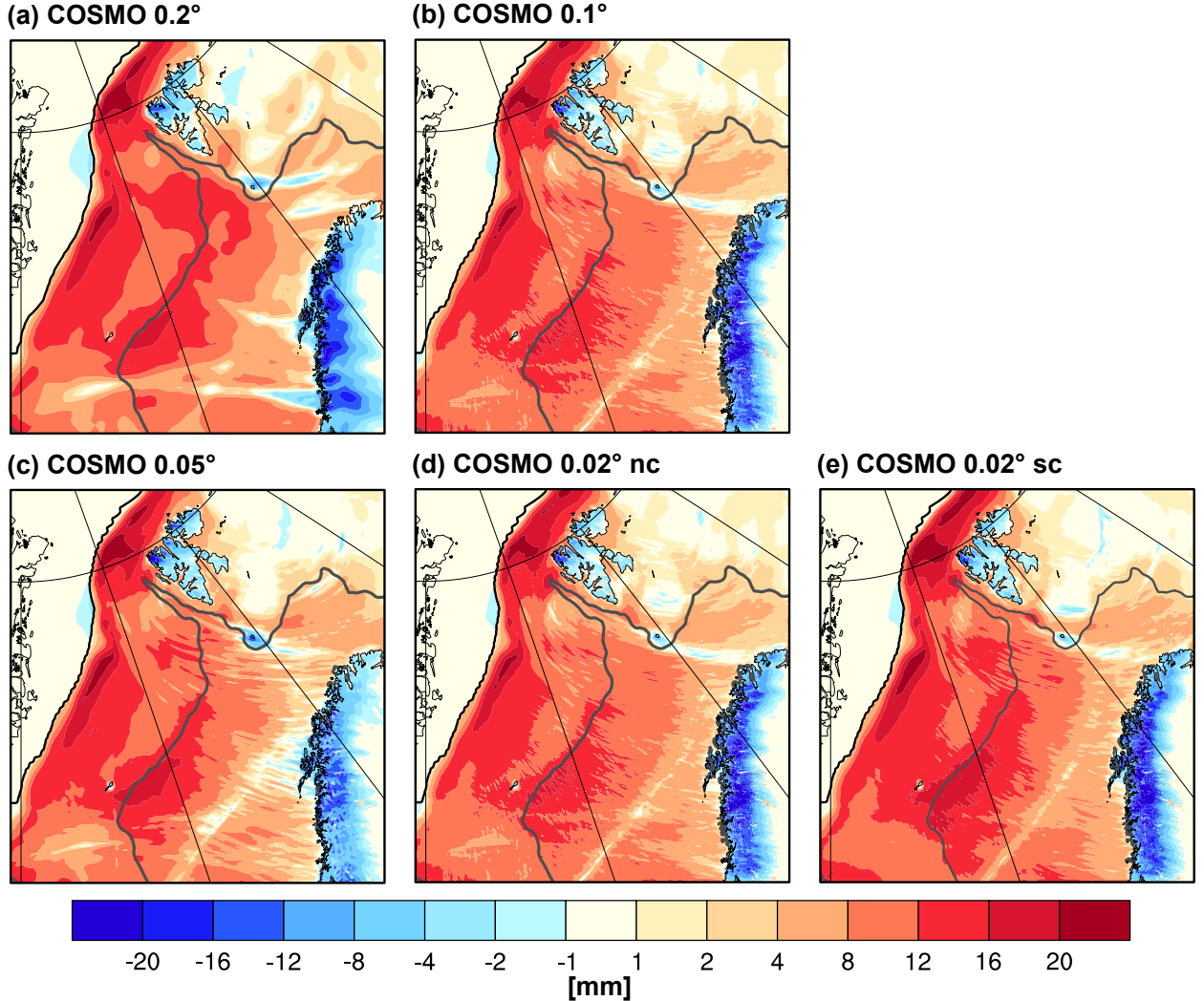
(a) Greenland, Iceland and Norwegian Seas



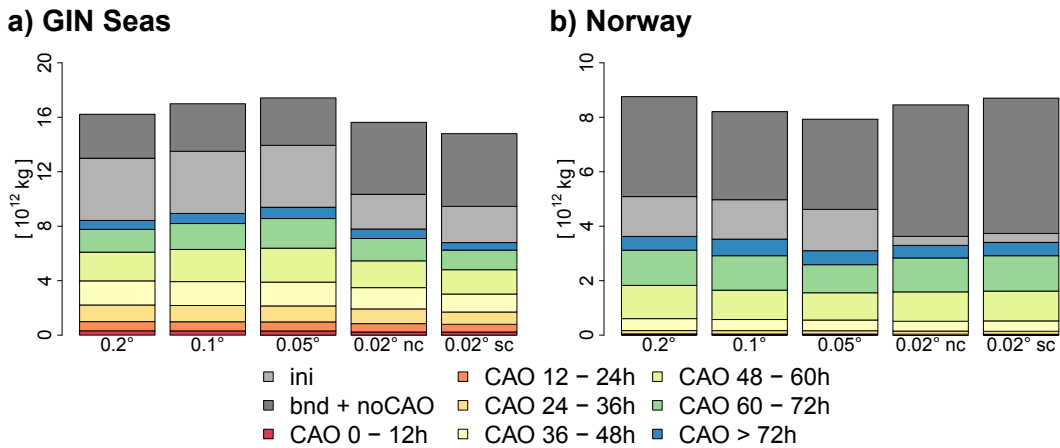
(b) Norway



1035 FIG. 12. Residence time of waters in tagged CAO precipitation expressed as fractions of total CAO precipi-
 1036 tation from 1800 UTC 23 Dec (+6 h) to 0000 UTC 27 Dec (+84 h) (a) in the Greenland, Iceland and Norwegian
 1037 Seas (GIN box, Fig. 1a) and (b) over Norway (NOR box, Fig. 1a) for simulations (from left to right) at res-
 1038 olutions of $0.2^\circ \times 0.2^\circ$, $0.1^\circ \times 0.1^\circ$, $0.05^\circ \times 0.05^\circ$, and $0.02^\circ \times 0.02^\circ$, the latter both for simulations without
 1039 (nc) and with (sc) shallow convection scheme active. Note that these estimates represent upper limits for the
 1040 residence time (cf. Section 2).



1041 FIG. 13. Footprints of tagged CAO evaporation minus precipitation for simulations at (a)
1042 $0.2^\circ \times 0.2^\circ$, (b) $0.1^\circ \times 0.1^\circ$, (c) $0.05^\circ \times 0.05^\circ$, and (d, e) $0.02^\circ \times 0.02^\circ$ without (nc) and with (sc) shallow
1043 convection scheme active, respectively. Fields are accumulated over the 78 h period between 1800 UTC 23 Dec
1044 (+6 h) to 0000 UTC 27 Dec (+84 h). To facilitate comparison, all fields are shown for the nested domain of the
1045 simulations at $0.02^\circ \times 0.02^\circ$ resolution. The 277 K isotherm of SST is drawn to illustrate the location of the
1046 Arctic front (gray line). Cold waters are located to the west and north of this line.



1047 FIG. 14. Accumulated tagged precipitation integrated over (a) the Greenland, Iceland and Norwegian Seas
 1048 (GIN box, Fig. 1a) and (b) Norway (NOR box, Fig. 1a) for simulations (from left to right) at $0.2^\circ \times 0.2^\circ$,
 1049 $0.1^\circ \times 0.1^\circ$, $0.05^\circ \times 0.05^\circ$, and $0.02^\circ \times 0.02^\circ$ resolution without (nc) and with (sc) shallow convection scheme
 1050 active. The accumulation is from 1800 UTC 23 Dec (+6 h) until 0000 UTC 27 Dec (+84 h). Contributions
 1051 are shown separately for initial vapor (light gray), vapor entering the domain from the boundary or the surface
 1052 outside of the CAO mask (dark gray), and vapor of CAO origin released in 12-hourly intervals (color).